Materials & Design 264 (2026) 115719

Contents lists available at ScienceDirect

Materials & Design

journal homepage: www.elsevier.com/locate/matdes

Low-temperature Fe–N enabled austenite stabilization in nickel-free nitrogen-alloyed stainless steels

Wei Hock Teh [a,b,*], Jing Jun Lee [a], Li Tian Chew [a], Kok Heng Cheong [a,c], Yakai Zhao [a,c], Baisong Cheng [a,c,*], Fengxia Wei [a,d], Tim J. White [b], Cheng Cheh Tan [a,c,*]

[a] Institute of Materials Research and Engineering (IMRE), Agency for Science, Technology and Research (A*STAR), 2 Fusionopolis Way, Innovis #08–03, 138634, Singapore
[b] School of Materials Science and Engineering, Nanyang Technological University, 639798, Singapore
[c] Future Energy Acceleration & Translation (FEAT), Agency for Science, Technology and Research (A*STAR), 2 Fusionopolis Way, Innovis #08-03, Singapore 138634 Singapore
[d] Mark Wainwright Analytical Centre, University of New South Wales, Sydney, NSW 2052, Australia

ARTICLE INFO

Keywords:
Nickel-free stainless steel
Nitrogen alloying
Additive manufacturing
Laser powder bed fusion (LPBF)
Interstitial solid-solution strengthening

ABSTRACT

Nickel-stabilized austenitic stainless steels are widely used but increasingly constrained by economic, environmental, and health concerns. Nitrogen offers a sustainable alternative austenite stabilizer; however, its low solubility in molten steel and high volatility complicate incorporation under ambient pressure. Here, we demonstrate a viable laser powder bed fusion (LPBF) materials-by-design approach to fabricate nickel-free, nitrogen-alloyed stainless steels using iron nitride (Fe−N) as a low-temperature nitrogen source under ambient condition. Optimized processing achieved near-full density (>99.5%) and retained up to ~0.45 wt% nitrogen, producing predominantly γ-austenite microstructure (~93%) with minor δ-ferrite. X-ray diffraction and electron microscopy detected no secondary nitrides within diffraction limits, while systematic lattice expansion indicated interstitial solid-solution strengthening. The resulting alloys exhibit high strength (YS ≈ 744–882 MPa, UTS ≈ 935–1062 MPa) with tunable ductility (El ≈ 10–21%), and modified corrosion behaviour relative to nitrogen-free counterparts, consistent with nitrogen-enhanced passivation. Although performance remains below that of Cr–N alloyed steels and SS316L, this approach avoids high-pressure processing and demonstrates that Fe–N precursors can effectively deliver nitrogen effectively during LPBF. These findings provide a foundation for the future optimization of sustainable, nickel-free stainless steels relevant to biomedical, energy, and structural systems.

1. Introduction

Stainless steels are indispensable in infrastructure [1–5], energy systems [6–10], and biomedical applications [11–14], with their corrosion resistance arising from chromium's passive oxide film. Among these, austenitic Fe–Cr–Ni grades (300-series) dominate production owing to their nickel-stabilized γ-austenite (face-centered cubic, FCC), which suppresses δ/α-ferrite (body-centered cubic, BCC) formation and enables excellent corrosion resistance, weldability, and strength [15–20].

However, the reliance on nickel introduces challenges. Economically, nickel exhibits strong price volatility and is geographically concentrated [21,22]. Medically, nickel hypersensitivity affects a significant population fraction [23–25]. In nuclear settings, Ni undergoes transmutation and segregation that degrades long-term performance [26]. Collectively, these concerns motivate the development of nickel-free austenitic stainless steels that retain the desirable attributes of the 300-series alloys.

Nitrogen has emerged as an effective and sustainable substitute for nickel [11,27–44]. As an interstitial austenite stabilizer, it strengthens the FCC lattice, suppresses martensite formation, and provides solid-solution strengthening of approximately 70–100 MPa per 0.1 wt% N, without the sensitization risk associated with carbon [36,45]. Beyond mechanical strengthening, nitrogen enhances corrosion resistance by enriching chromium oxide film and accelerating repassivation, enabling conventionally processed Ni-free steels to outperform 316 L in body

* Corresponding authors at: Institute of Materials Research and Engineering (IMRE), Agency for Science, Technology and Research (A*STAR), 2 Fusionopolis Way, Innovis #08–03, 138634, Singapore.
E-mail addresses: gary_teh@a-star.edu.sg (W.H. Teh), cheng_baisong@a-star.edu.sg (B. Cheng), dennis_tancc@a-star.edu.sg (C.C. Tan).

https://doi.org/10.1016/j.matdes.2026.115719
Received 10 November 2025; Received in revised form 3 February 2026; Accepted 23 February 2026
Available online 24 February 2026

fluids and marine environments [35,46–48]. Abundant, non-toxic, and inexpensive, nitrogen is therefore highly attractive for sustainable alloy design.

Despite these advantages, nitrogen's low solubility in molten iron (~0.05 wt% N in Fe at 1600 °C) and its volatility under ambient pressure severely limit uptake, historically necessitating high-pressure metallurgy or specialized processing routes [49–51]. Manganese partially alleviates this limitation by stabilizing γ-austenite and increasing nitrogen solubility. For example, in Fe–20Cr–20Mn, nitrogen solubility can reach ~0.6 wt% at 1600 °C, compared to ~0.05 wt% in pure Fe [52]. Consequently, Fe–Cr–Mn–N alloys have become the compositional backbone of modern nickel-free austenitic steel.

Additive manufacturing, particularly laser powder bed fusion (LPBF), offers a fundamentally different paradigm for alloy design. Beyond geometric freedom, LPBF offers unique advantages for stainless steel design through localized melting, extreme thermal gradients, and ultrafast cooling rates (10^3–10^8 Ks^{-1}). These non-equilibrium conditions enable solute trapping, refined cellular substructures, high dislocation densities, and controllable γ/δ phase balance, allowing access to microstructures that are difficult or impossible to achieve via conventional processing [53]. Importantly for nitrogen-alloyed systems, the short melt-pool lifetime and rapid solidification inherent to LPBF provide a kinetic pathway for retaining volatile interstitial elements such as nitrogen under ambient pressure. As a result, LPBF can be leveraged not only as a shaping technology but as a materials-by-design platform for tuning mechanical and corrosion properties of stainless steel.

Multiple nitrogen-introduction strategies have been examined – from nitrogen-atomized powders [54] or as-atomized N-bearing powders [55–59] and nitrogen-rich shielding gases [60], to nitrogen steel wire feedstocks [61–66] or ceramic nitrides addition such as Si_3N_4 [67] and Cr−N [68,69]. Collectively, these methods demonstrate nitrogen uptake, but they face practical limits. Gas-based routes depend strongly on atmosphere control; pre-alloyed powders require specialized atomization; and ceramic nitrides often exhibit poor flowability and high decomposition temperatures (e.g., Cr−N ≈900 °C), impairing densification and promoting nitrogen loss under LPBF's intense thermal gradients. Reported porosity of 0.5–3% and limited nitrogen retention remains barriers to scalability [68,69].

A low-temperature, composition-tunable nitrogen source therefore remains an unmet need. Here, we introduce iron nitride (Fe−N) as such a precursor, engineered to synchronize nitrogen release with LPBF's thermal cycle. Fe−N decomposes between ~450–680 °C [70], releasing nitrogen early in the thermal cycle, enabling nitrogen dissolution into the transient melt before peak temperatures are reached. Unlike ceramic nitrides, Fe−N fully dissolves within the metallic matrix, avoiding undissolved residues that degrade flowability or mechanical response. This thermodynamic–kinetic approach enables efficient interstitial nitrogen trapping under ambient pressure, forming the basis for our Fe–N assisted LPBF design strategy.

In this work, we systematically investigate the design logic of Fe−N assisted LPBF of Fe–Cr–Mn stainless steels and map the process–composition–microstructure–property links that govern nitrogen retention, γ-austenite / δ-ferrite balance, and final mechanical and corrosion properties. By validating an ambient-pressure, non-equilibrium route to nitrogen supersaturation, this study demonstrates a scalable materials-by-design pathway for sustainable, nickel-free stainless steels, providing a foundation for future process and compositional optimization relevant to biomedical, structural, and energy systems.

2. Experimental procedure

2.1. Powders and blending

Gas-atomized Fe–Mn, Fe–Cr, and Fe–N powders were blended to formulate a nickel-free, high-manganese feedstock designed for γ-austenite stability. The Fe–Mn (49.6 wt% Mn, 20–60 μm), Fe–Cr (46.2 wt% Cr, 20–60 μm), and Fe–N (6.7 wt% N, <20 μm) powders were mixed at 150 rpm for 24 h using zirconia media to achieve a nominal Fe–18Cr–20Mn–1.3 N (wt%) feedstock. The blend recipe is given in Table 1; detailed powder characteristics are provided in Supplementary Information **SI Fig. S1** and **SI Table S1**. Powder X-ray diffraction (XRD) confirmed Fe–Mn to exhibit a FCC crystal structure, Fe–Cr a BCC crystal structure, and Fe–N a mixed $Fe_3N/Fe_{12}N_5/Fe_4N$ phases.

2.2. LPBF fabrication

LPBF processing was conducted on a BLT-S210 LPBF system under high-purity argon atmosphere. Two specimen geometries were fabricated: 10 × 10 × 10 mm cubes for process-parameter mapping and microstructural analysis, and 48 × 12 × 10 mm bars with 67° rotation between layers for tensile testing (**SI Fig. S2**).

Process variables were systematically explored: laser power (50–450 W), scan speed (250–2000 mm s^{-1}), and hatch spacing (0.08–0.15 mm). Layer thickness and beam diameter were fixed at 30 μm and 100 μm, respectively. These parameters were explored to identify conditions that maximize densification while minimizing nitrogen volatilization.

2.3. Sample preparation and characterization

Built samples were sectioned using wire electric discharged machining (EDM), mechanically ground, and mirror-polished to 0.03 μm finish. Phase morphologies were revealed by chemical etching ($6H_2O$ + HNO_3 + 2HCl by volume). Unetched surfaces were used for porosity measurements.

Porosity was determined by optical image analysis (Olympus BX53M Microscope) of polished cross-sections. Multiple fields of view were acquired per sample, and pore area fractions were quantified using threshold segmentation to obtain an average relative density.

Bulk chemical compositions were measured by optical emission spectrometry (spark-OES, Hitachi OE750), with local variations mapped via energy dispersive X-ray spectroscopy (EDX, JEOL JSM-7600F). Nitrogen was quantified using inert-gas-fusion (IGF, ASTM E1019) for high-accuracy assessment under varying process conditions.

Thermal decomposition of Fe–N powders was characterized using differential scanning calorimetry/thermogravimetry (DSC/TGA, NETZSCH STA449 F1 Jupiter) from 50 to 1400 °C at 10 °C min^{-1} under argon (Al_2O_3 crucible). The data established the temperature window (≈450–680 °C) for nitrogen release relevant to the LPBF thermal cycle.

Phase constitution and lattice parameters were quantified by laboratory X-ray diffraction (Bruker D8 Advance, Cu Kα, λ = 1.5406 Å, 2θ = 20–100°) with Rietveld analysis using TOPAS v5). To enhance sensitivity to minor secondary phases, selected samples were examined by high-resolution synchrotron XRD at the Australian Synchrotron (λ = 0.688678 Å, calibrated using NIST LaB_6 standard material). This approach enables detection of crystalline secondary phases down to low volume fractions; however, nanoscale precipitates below diffraction detection limits cannot be fully excluded. Austenite/ferrite phase fractions were determined from Rietveld analysis and independently cross-validated using electron backscatter diffraction (EBSD).

EBSD was performed using a JEOL IT500HR microscope equipped with an Oxford Symmetry detector. Data was processed in AZtecCrystal to obtain inverse pole figure (IPF), phase, and geometrically necessary dislocation (GND) density maps, used here as a proxy for dislocation substructures formed during LPBF.

Mechanical properties were assessed at multiple scales: Vickers microhardness (InnovaTest Falcon 5000, 1 kgf/15 s), nanoindentation across FCC/BCC regions (KLA-Tencor G200, Berkovich), and tensile testing of machined bars with video extensometer (INSTRON 5900R, 0.3 mm min^{-1}).

Corrosion properties were assessed using potentiodynamic polarization performed in 3.5 wt% NaCl electrolyte at room temperature

Table 1
Nominal compositions, blend ratios, and calculated elemental concentrations of the powder mixtures used in this study.

Powder	Ratio (wt%)	Composition (wt%)									
		Fe	Cr	Mn	N	C	Si	P	S	Mo	O
Fe–Mn	40	Bal.	–	49.60	–	0.02	0.36	<0.01	0.02	–	0.04
Fe–Cr	39	Bal.	46.20	–	–	0.02	0.75	<0.01	0.02	–	0.06
Fe–N	21	Bal.	–	–	6.7	–	–	–	–	–	–
Blended powder	100	Bal.	18.02	19.84	**1.26**	0.02	0.44	0.01	0.02	0.00	0.04

(Metrohm Autolab PGSTAT300) in a three-electrode cell (Pt counter, Ag/AgCl 3 M KCl reference). Samples with 1 cm^2 exposed area were held at open circuit potential (OCP) for 120 min before scanning from −0.2 V to +1.0 V vs OCP at 1 mV s^{-1}.

2.4. Reference materials: Fe−Cr−Mn (Ni-free N-free), Fe−Cr−Mn−N (alloyed using Cr-N), SS304 and SS316L

For benchmarking, Fe−N builds developed in this work were compared against LPBF-processed reference alloys:

(i) Ni-free, N-free Fe–Cr–Mn stainless steel [68],
(ii) Cr–N-alloyed Fe–Cr–Mn–N stainless steel [68], and
(iii) conventional austenitic stainless steel SS304 and SS316L fabricated by LPBF.

The Ni-free, N-free Fe–Cr–Mn alloy comprised approximately Fe–18Cr–24Mn (wt%) with no intentional nitrogen addition. The Cr–N-alloyed Fe–Cr–Mn–N reference had a similar Fe–Cr–Mn base composition but contained ~0.87 wt% N introduced via Cr–N addition, representing a nitrogen-rich benchmark achieved using ceramic nitride precursors.

Commercial LPBF SS304 is a Mo-free austenitic stainless steel containing ~18–20 wt% Cr, 8–12 wt% Ni, and < 0.1 wt% N, while LPBF SS316L contains ~16–18 wt% Cr, 10–14 wt% Ni, 2–3 wt% Mo, and < 0.1 wt% N. SS304 provides a compositionally closer Mo-free austenitic reference for comparison with the present Fe–N alloys, whereas SS316L serves as a widely used performance benchmark with enhanced corrosion resistance due to Mo addition.

The full nominal compositions are summarized in Table 2 for direct comparison with the Fe–N alloys developed in this work.

3. Results

3.1. A low-power LPBF window maximizes density while preserving nitrogen

To identify processing conditions that simultaneously enable near-full density and effective nitrogen retention, laser power (P), scan speed (v), and hatch spacing (h) were systematically varied at fixed layer thickness and beam diameter (Fig. 1, full dataset in **SI Table S2,** etched microstructures in **SI Fig. S3-S4**, additional analysis in **SI Fig. S5**). For each parameter set, relative density, chemical composition, phase fractions, and hardness were evaluated.

Relative density was quantified from polished cross-sections using optical microscopy combined with image analysis, in which the pore area fraction was quantified from polished cross-sections using threshold-based image analysis. Bulk chemical composition, including nitrogen content, was initially measured using spark-OES. As the instrument was not calibrated for the full nitrogen range, these values were used only to track compositional trends. For accurate quantification, representative samples were subsequently analyzed by inert-gas fusion (IGF), and those values are reported and discussed in later sections. Phase constitution and FCC/BCC phase fractions were quantified by Rietveld refinement of XRD diffraction patterns, with the results cross-validated by EBSD phase mapping.

The coupled responses of densification and nitrogen retention were mapped across a broad volumetric energy density (VED, **(Eq. *(1)***) range of ~22–600 J mm^{-3} (Fig. 2a).

$$VED\left(\frac{J}{mm^3}\right) = \frac{P(W)}{v\left(\frac{mm}{s}\right) \times h(mm) \times t(mm)} \quad (1)$$

At low laser power (P ≤ 100 W), insufficient energy input led to lack-of-

Table 2
Composition, density, hardness and phase fractions of LPBF-processed samples fabricated under different process conditions, together with reference alloys. * Indicates that N content reported was measured using inert gas fusion technique; the rest of elements were measured using Spark-OES (n = 5, SD < 0.1 wt%). Chemical composition of SS316L is based on materials datasheet.

Method	Sample	Laser Power	Fe	Cr	Mn	N	Ni	C	Si	P	S	Mo	Ref
		(W)	(wt%)	(wt%)	(wt%)	(wt%)	(wt%)	(wt%)	(wt%)	(wt%)	(wt%)	(wt%)	
LPBF	Ni free, N free	175	Bal.	19.3	22.6	–	–	0.02	0.6	0.01	0.01	–	[68]
LPBF	Ni free, Cr-N	175	Bal.	19.0	20.2	0.87*	–	0.02	0.01	0.01	0.01	–	[68]
LPBF	SS316L	120	Bal.	16.5–18.5	2.0	0.10	10–13	0.03	0.75	<0.01	<0.01	2.0–2.5	[73]
LPBF	Ni free, Fe-N	450	Bal.	18.59	18.48	0.27*	–	0.05	0.42	0.01	0.01	–	This work
LPBF	Ni free, Fe-N	350	Bal.	18.45	19.92	0.33*	–	0.05	0.42	0.01	0.01	–	This work
LPBF	Ni free, Fe-N	250	Bal.	18.51	19.57	0.36*	–	0.06	0.44	0.01	0.01	–	This work
LPBF	Ni free, Fe-N	150	Bal.	19.11	19.75	0.45*	–	0.06	0.47	0.01	0.01	–	This work

Method	Sample	Laser Power (W)	Density (%)	Hardness (HV)	FCC (wt%)	FCC Lattice Parameters (Å)	BCC (wt%)	BCC Lattice Parameters (Å)	Ref
LPBF	Ni free, N free	175	99.89	266 ± 13	9.91 (17)	3.615(13)	90.09 (7)	2.87777(4)	[68]
LPBF	Ni free, Cr-N	175	99.54	384 ± 16	100	3.638(74)	–	–	[68]
LPBF	SS316L	120	99.94	224 ± 5	100	3.60095(61)	–	–	[73]
LPBF	Ni free, Fe-N	450	99.82	325 ± 13	66.5(2)	3.61619(17)	33.5(2)	2.88135(16)	This work
LPBF	Ni free, Fe-N	350	99.75	344 ± 11	77.27(19)	3.61946(18)	22.73(19)	2.88177(17)	This work
LPBF	Ni free, Fe-N	250	99.71	342 ± 12	75.6(3)	3.62127(18)	24.4(3)	2.8828(2)	This work
LPBF	Ni free, Fe-N	150	99.60	326 ± 19	92.89(18)	3.6268(3)	7.11(18)	2.8863(4)	This work

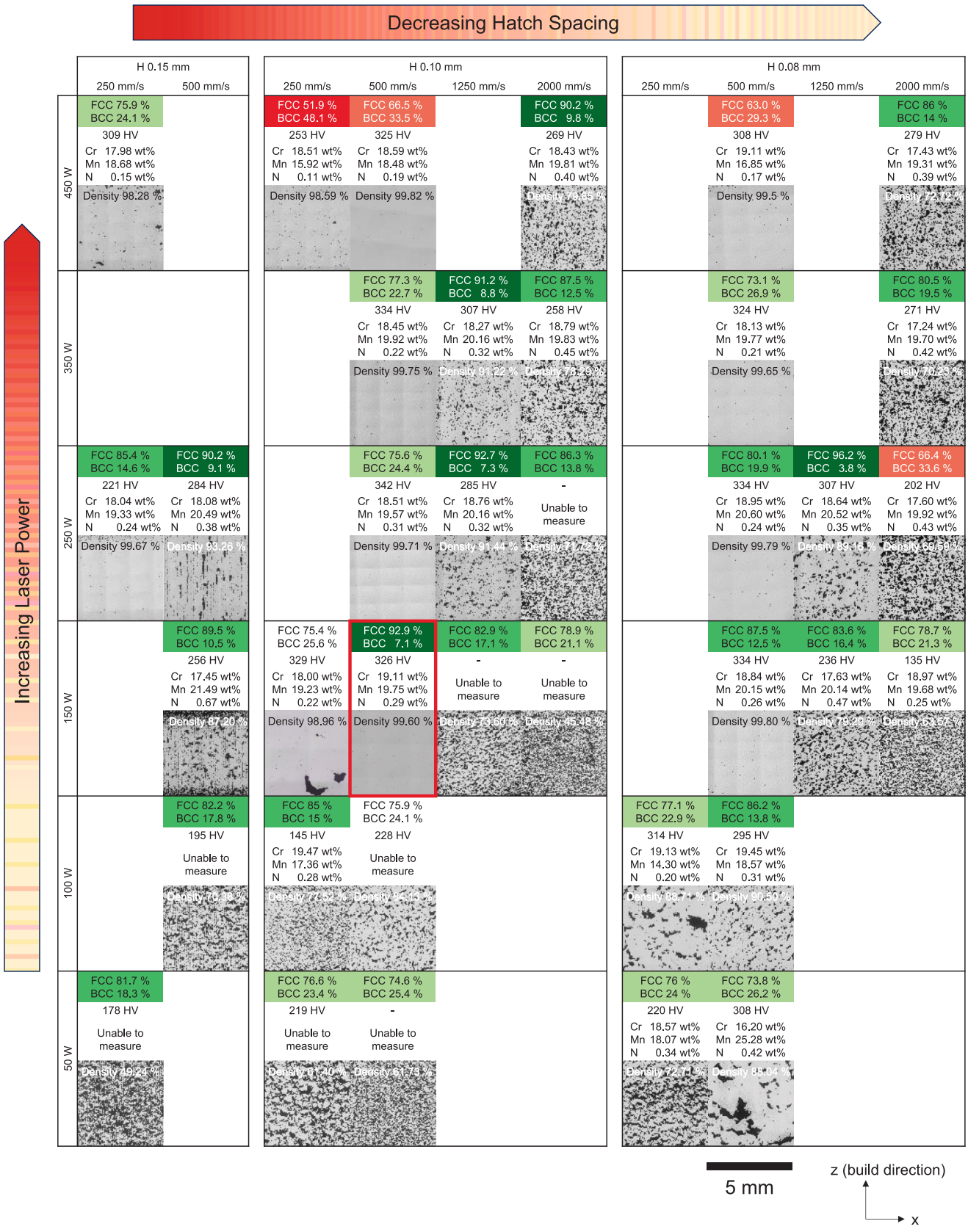

Fig. 1. Influence of LPBF processing parameters on densification and nitrogen retention. Relative density, elemental composition, phase fractions, and hardness as a function of laser power, scan speed, and hatch spacing.

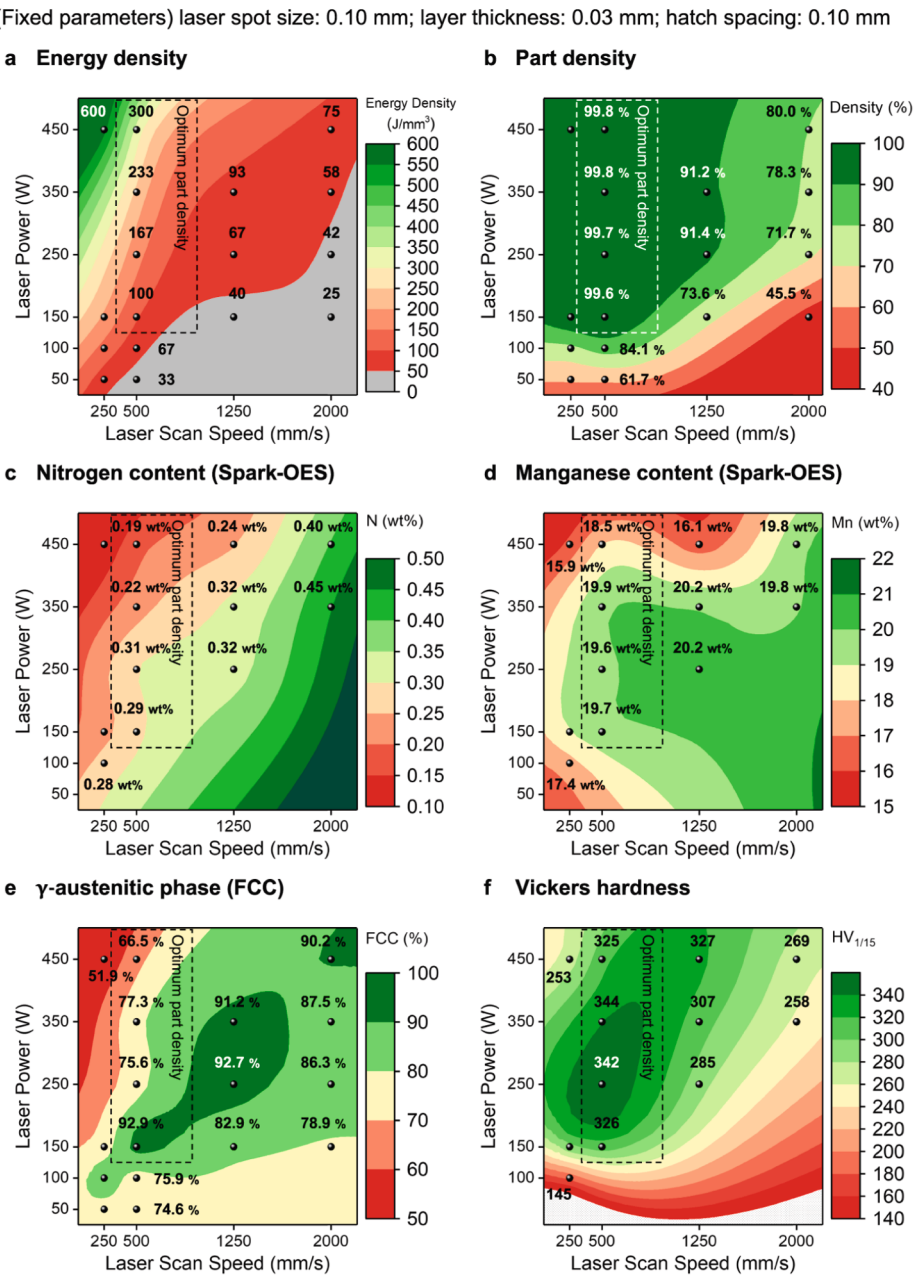

Fig. 2. Effect of laser power and scan speed on (a) energy density, (b) part density, (c) nitrogen content, (d) manganese content, (e) γ-austenitic content and (f) Vickers hardness at fixed laser spot size (0.10 mm), layer thickness (0.03 mm) and hatch spacing (0.10 mm).

fusion porosity, with densities falling below 84.1% and in extreme cases approaching 61.7% (Fig. 2b). Increasing power improved consolidation; however, excessive power progressively reduced retained nitrogen and manganese despite high density, consistent with volatilization loss. For example, at P = 450 W, retained N fell to ~0.19 wt% and the γ-austenite fraction declined to ~51.9–66.5%. (Fig. 2**c-e**).

Scan speed (v) exerted a strong influence on both densification and nitrogen retention. At fixed P, reducing v enhanced melt consolidation but penalized N retention unless balanced by P or hatch spacing (h). A moderate speed of v ≈ 500 mm s^{-1} at P = 150–250 W balanced these effects, delivering dense parts (>99.5%) with spark-OES N ≈ 0.29–0.31 wt% (**SI Fig. S6**).

Hatch spacing further modulated thermal accumulation. Excessively large h produced lack-of-fusion porosity, whereas overly small h increased remelting and nitrogen volatilization. Matching h to the melt-pool width provided full track overlap without excessive re-melt. The optimal condition was identified near P = 150 W, v = 500 mm s^{-1}, and h = 0.10 mm, yielding > 99.5% density with ~0.29 wt% nitrogen by spark-OES and a γ-austenite fraction approaching 93%.

These results demonstrate that nitrogen retention is governed primarily by melt-pool thermal history rather than volumetric energy density alone. Operating at moderate power minimizes volatilization while ensuring adequate fusion, enabling simultaneous densification and nitrogen uptake.

3.2. Fe-N delivers ~0.27–0.45 wt% nitrogen without secondary nitrides, shift phase balance to up to 93% γ-austenite (FCC), raise hardness by ~25%

During process mapping (**Section 3.1**), bulk chemical composition was quantified using spark-OES. Due to the wide range of nitrogen content, the OES equipment was not calibrated for the full range of

nitrogen content. Therefore, IGF was used for precise quantitative testing of retained nitrogen content on representative builds (**SI Table S3**). For subsequent analyses, IGF-measured nitrogen contents are reported as the composition of record (Table 2).

The blended feedstock contained a nominal 1.26 wt% N and 19.84 wt% Mn. Fabricated samples retained 0.27 to 0.45 wt% N, depending on laser power (Table 2). At low power (150 W), samples retained the highest nitrogen (~0.45 wt%) with near-nominal Mn (~19.75 wt%). As power increased to 450 W, nitrogen dropped toward ~0.27 wt% alongside reduced Mn (~18.48 wt%), despite densities remaining above 99.5%.

Rietveld analysis of laboratory XRD patterns revealed only γ-austenite (FCC) and δ-ferrite (BCC) across the processing window. No reflections of Cr–N, Fe–N, or related nitride families were detected. Additional high-resolution synchrotron scans of the high-N, high-γ state likewise showed no nitride peaks above background (Fig. 3). Within the detection limits laboratory and synchrotron diffraction (~5–10%) [71,72], these results indicate that nitrogen is retained predominantly in solid-solution rather than as discrete nitride precipitates.

Phase analysis showed nitrogen enrichment directly promoted γ-austenite stability (Fig. 4a), raising hardness by ~25% (Fig. 4b). As shown in Fig. 4a, the γ-austenite fraction increases with nitrogen content and approaches a saturation plateau at high N. Within the experimentally accessible Fe–N LPBF window (0.27–0.45 wt% N), the FCC fraction exhibits an approximately linear dependence on nitrogen content ($R^2 \approx 0.95$), which may be expressed as:

$$f_\gamma(\%) = 143N(wt\%) + 28 (R^2 \approx 0.95) \quad (2)$$

Corresponding to an increase of ~14–15% FCC for every 0.10 wt% increase in nitrogen. With the BCC fraction given by:

$$f_\delta(\%) = 100 - f_\gamma \quad (3)$$

At higher nitrogen contents (Cr–N reference alloys, N ≈ 0.9–1.1 wt%), the FCC fraction approaches a saturation plateau of ~95–100%, consistent with the bounded nature of phase fractions. This trend is consistent with the strong austenite-stabilizing effect of interstitial nitrogen and highlights diminishing returns once near-single-phase FCC is achieved.

Lattice parameter analysis further supported interstitial N rather than nitride precipitation: the FCC lattice expanded by ~0.40% (Δa ≈ +0.015 Å) at ~0.45 wt% N (Fig. 4c), whereas the BCC lattice varied only weakly by ~0.29% with composition (Δa ≈ +0.008 Å, Fig. 4d).

Microstructural imaging found no evidence of nitride dispersions at the resolution of EBSD; grains were larger in high γ-austenite state, with smaller grains and more δ-ferrite grains as power increased, mirroring the diffraction trend (Fig. 5). Elemental maps showed Fe/Cr/Mn homogeneity and only qualitative N contrast, as expected near the EDX sensitivity limit; these maps were used for uniformity screening rather than quantification (**SI Fig. S7**).

Nanoindentation maps confirmed the increase in hardness in both γ-austenite (FCC) and δ-ferrite (BCC) regions for the higher-N state, with comparable spread, consistent with interstitial strengthening rather than the emergence of a hard second phase (Fig. 6).

Taken together, these findings demonstrate that Fe–N precursors enable significant interstitial nitrogen uptake (~0.45 wt%), stabilize γ-austenite fractions approaching 93%, and enhance hardness by ~25%, all without detectable secondary nitrides.

3.3. Grain refinement with increasing laser power

Increasing laser power promotes δ-ferrite formation and systematic grain refinement. Raising laser power reorganized the microstructure from predominantly γ-austenite (FCC) to a dual-phase γ/δ state (Fig. 5). Grain sizes in both phases reduce with increasing power: maximum γ-austenite size decreased from ~17 μm at 150 W to ~7 μm at 450 W, while δ-ferrite grains refined from ~11 to ~6 μm over the same range (**SI Fig. S8**). Both phases maintained elongated grain shape with aspect ratios of ~2, characteristic of directional solidification under LPBF conditions.

In parallel with grain refinement, γ-austenite exhibits a progressive increase in geometrically necessary dislocation (GND) density, rising from $1.9 \pm 0.9 \times 10^{14}$ m^{-2} at 150 W (9.0 ± 8.2 μm grains) to $2.6 \pm 0.9 \times 10^{14}$ m^{-2} at 450 W (5.1 ± 1.9 μm grains). This increase reflects the development of LPBF-induced cellular dislocation substructures, where dislocation cell walls form on the submicron scale under extreme thermal gradients and rapid solidification. In contrast, δ-ferrite exhibits relatively constant GND (~$2.1–2.2 \times 10^{14}$ m^{-2}), consistent with its already fine and stable grain size distribution (**SI Fig. S8**).

Overall, increasing laser power refines both γ and δ grains while selectively elevating dislocation density in γ-austenite. The emergence of δ-ferrite under the present LPBF conditions coincides with restricted γ grain growth and the formation of a finer dual-phase microstructure characterized by hierarchical grain and sub-grain scale features.

3.4. Mechanical performance

Tensile testing reveals a tunable strength–ductility balance governed by the relative fractions of γ-austenite and δ-ferrite (Table 3, Fig. 7). In the γ-rich condition (150 W; ~93% γ, 0.45 wt% N), specimens achieved YS = 744 ± 42 MPa, UTS = 935 ± 57 MPa, and elongation = 20.8 ± 3.9%. At higher power (450 W; ~67% γ, 0.27 wt% N), strength increased to YS = 882 ± 80 MPa and UTS = 1062 ± 44 MPa, but elongation declined to 10.5 ± 4.3%. Replicate statistics and full stress–strain curves are provided in **SI Table S4** and **SI Fig. S9**.

Relative to reference alloys, the Fe–N pathway exhibits distinct mechanical trade-offs. Compared with the Ni-free, N-free build (YS ≈ 498 MPa, UTS ≈ 604 MPa, El ≈ 15%), retaining nitrogen in the γ-rich state improves strength by ~55% and ductility by ~38%. In comparison with Cr–N alloyed builds at higher N (~0.87 wt%), the 150 W state offered higher ductility at slightly lower strength, whereas the 450 W state surpassed prior UTS values at the expense of elongation. For context, LPBF SS316L displays high ductility (El ≈ 59%) but substantially lower strength (YS ≈ 514 MPa, UTS ≈ 605 MPa).

These results establish that modest variations in retained nitrogen and resulting γ-austenite / δ-ferrite fractions enable systematic tuning of tensile properties. Ultimate tensile strength exceeding 1 GPa can be achieved while maintaining moderate ductility (~20%) under the

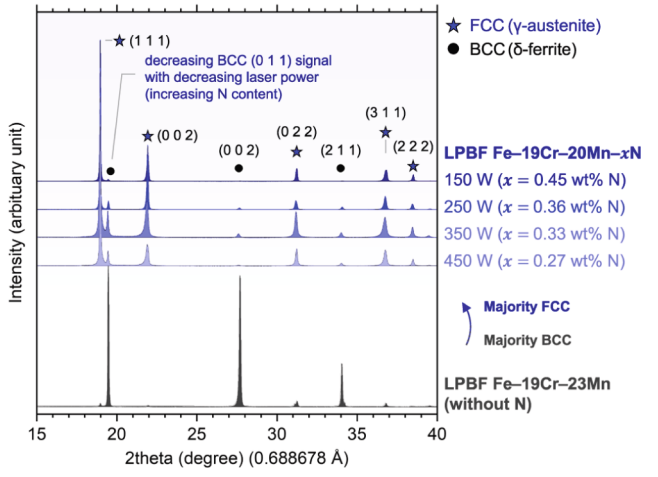

Fig. 3. Synchrotron X-ray diffraction patterns of LPBF-processed Fe–19Cr–20Mn–xN alloys fabricated at different laser powers, together with the nitrogen-free Fe–19Cr–23Mn reference. Indexed reflections correspond to γ-austenite (FCC) and δ-ferrite (BCC).

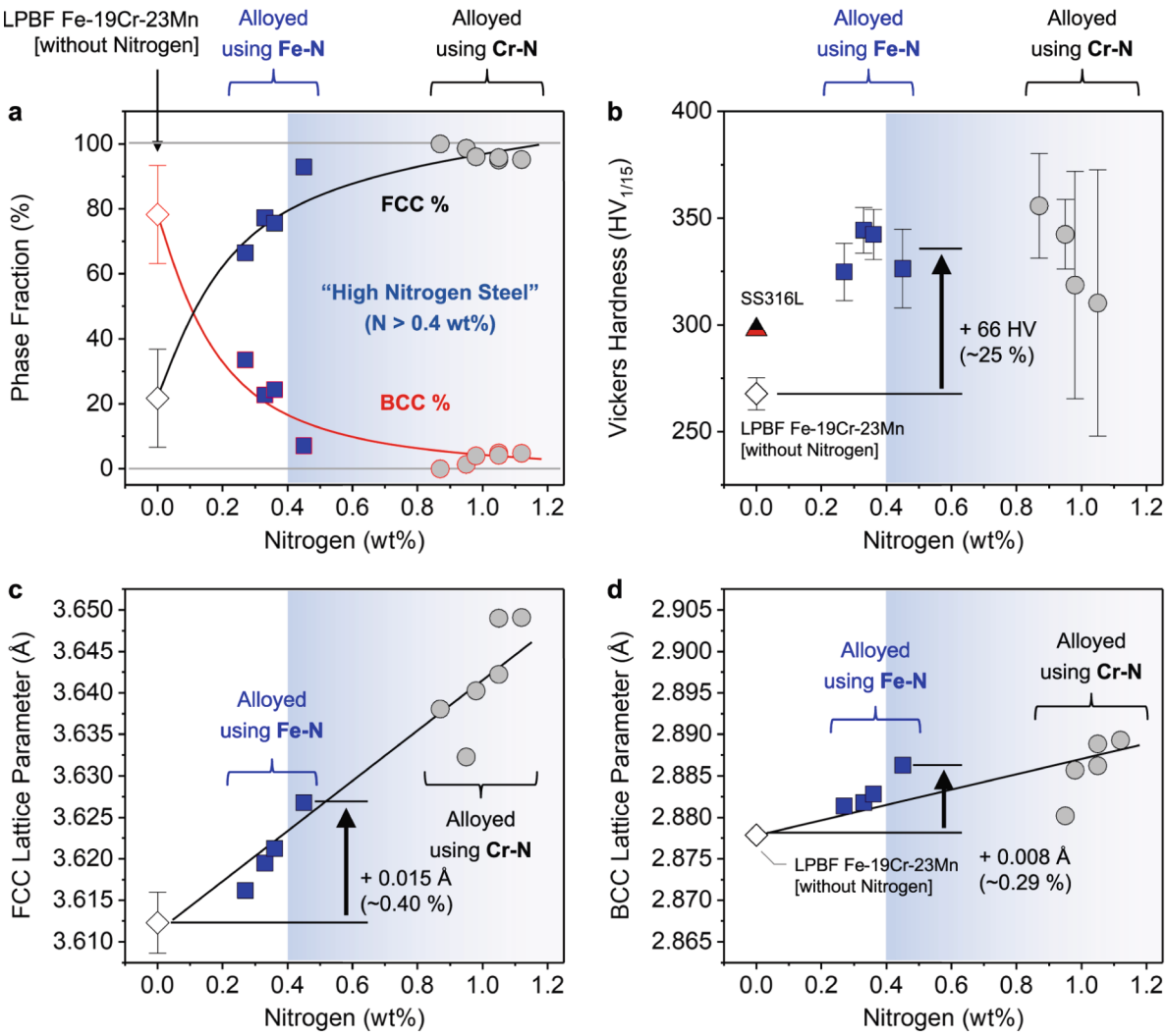

Fig. 4. Effect of nitrogen content on (a) phase balance, (b) Vickers hardness, (c) γ-austenite (FCC) lattice parameters and (d) δ-ferrite (BCC) lattice parameters.

present LPBF conditions, approaching the strength levels commonly associated with duplex stainless steels while retaining an austenite-dominated microstructure and avoiding secondary nitride formation.

3.5. Corrosion resistance performance

Potentiodynamic polarization was performed in 3.5 wt% NaCl using a three-electrode cell with Ag/AgCl (3 M KCl) as the reference electrode. Corrosion potential (E_{corr}) and corrosion current density (I_{corr}) were extracted from the polarization curves to compare general corrosion tendency, while the pitting potential (E_{pit}) and pitting current (I_{pit}) were used to evaluate localized corrosion resistance where a distinct breakdown was observed (Table 3, Fig. 8). Replicate statistics and full polarization curves are provided in **SI Table S5** and **SI Fig. S10**.

Among the stainless steel benchmarks, LPBF SS304 and LPBF SS316L exhibit the most noble corrosion potentials and the lowest general corrosion currents, with E_{corr} = –121 ± 0.3 mV and I_{corr} = 0.067 ± 0.007 μA cm^{-2} for SS304, and E_{corr} = –129 ± 9 mV and I_{corr} 0.121 ± 0.025 μA cm^{-2} for SS316L. Both alloys show stable passive behavior followed by pitting breakdown, with comparable pitting potentials (E_{pit} = 495 ± 32 mV for SS304 and E_{pit} = 474 ± 116 mV for SS316L). The associated pitting currents (I_{pit} = 2.936 ± 0.212 μA cm^{-2} for SS304 and I_{pit} = 3.740 ± 0.977 μA cm^{-2} for SS316L) indicate sustained pit propagation once breakdown occurred.

For the nickel-free reference alloys, the LPBF Fe–Mn–Cr (N-free) material displays a substantially more active response, with E_{corr} = –358 ± 30 mV and I_{corr} = 2.537 ± 1.422 μA cm^{-2}, reflecting weaker passivation and higher general dissolution relative to SS304 and SS316L. Mild steel exhibits the most active potential (E_{corr} = –689 ± 31 mV) and a measurable corrosion current (I_{corr} = 0.597 ± 0.431 μA cm^{-2}), consistent with the absence of stable passivation in chloride media.

Introducing nitrogen via ceramic nitride addition (Cr–N route) markedly improves electrochemical nobility and reduces general corrosion current relative to the Ni-free, N-free baseline. The LPBF Cr–N alloy showed E_{corr} = –134 ± 11 mV and I_{corr} = 0.159 ± 0.095 μA cm^{-2}, approaching the behavior of conventional austenitic stainless steels. A distinct pitting breakdown is observed with E_{pit} = 497 ± 69 mV and I_{pit} = 6.780 ± 3.920 μA cm^{-2}, indicating that while passivation is strong, localized breakdown under chloride exposure can occur once the critical potential is exceeded.

In contrast, the LPBF Fe–N alloy developed in this work exhibit more active corrosion potential (E_{corr} = –400 ± 33 mV) and higher general corrosion currents (I_{corr} = 2.736 ± 1.440 μA cm^{-2}) compared with Cr–N route and commercial austenitic references. This behavior is consistent with the presence of δ-ferrite and γ/δ phase heterogeneity, which promote micro-galvanic coupling and reduce passive film stability, as discussed in Section 4.5. Notably, no distinct stable pitting breakdown is observed for the Fe–N alloys within the tested potential window, suggesting that localized corrosion is dominated by metastable pit events rather than sustained pit growth. Despite the elevated I_{corr}, the

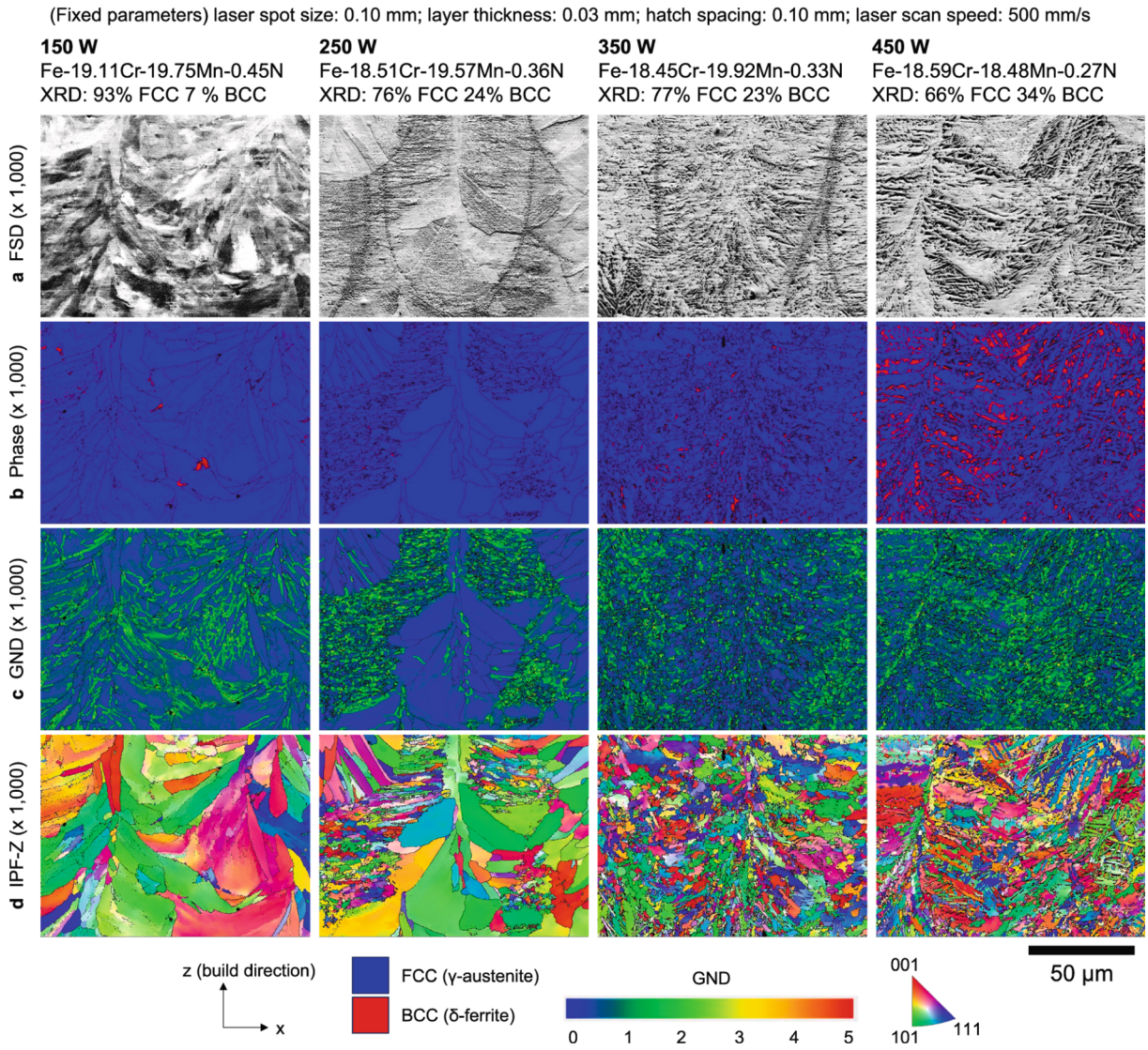

Fig. 5. EBSD characterization of LPBF-processed samples fabricated at different laser power. As shown are (a) forward-scattered electron (FSD) images, (b) phase maps, (c) geometrically necessary dislocation (GND) density maps, and (d) inverse pole figure (IPF) map, highlighting, γ-austenite (FCC) and δ-ferrite (BCC) distributions.

polarization response remains less active than that of mild steel, indicating that nitrogen addition still modifies interfacial electrochemistry relative to fully nitrogen-free alloys, albeit without achieving the passivation levels of Cr–N or Ni-containing stainless steels.

4. Discussion

4.1. Mechanism of nitrogen retention in LPBF using Fe–N precursors

During LPBF, Fe–N precursors decompose between ~450–680 °C [70] (**SI Fig. S11-12**), releasing nitrogen early in the transient thermal cycle. As powder ahead of the laser preheats through this temperature window, nitrogen is released and can dissolve into the forming melt pool, which reaches temperatures on the order of ~2000–3000 °C before cooling below ~500 °C on the order of ~1 s [76,77]. This brief liquid lifetime is crucial: operating at lower laser powers (~150 W) reduces recoil pressure and volatilization losses, favoring net nitrogen uptake. Subsequent rapid solidification traps nitrogen interstitially in the solid and biases the solidification path towards direct liquidus (L) → γ [78], consistent with the higher nitrogen solubility in γ-austenite (≤10.3 at% N, ~2.8 wt%) compared to δ/α-ferrite (≤0.4 at% N, ~0.1 wt%) [70].

Experimentally, inert-gas fusion confirms ~0.27–0.45 wt% nitrogen retention across the process map, peaking in the low-power window (Table 2). Retained nitrogen co-varies with manganese, consistent with their coupled solubility behavior in Fe–Cr–Mn melts. High-resolution synchrotron diffraction and EBSD identify γ-austenite and δ-ferrite as the dominant phases, with no nitride reflections detected within diffraction limits, while the systematic γ lattice expansion with nitrogen content and the strengthening response are consistent with nitrogen being predominantly accommodated in interstitial solid-solution (Figs. 3-8); nanoscale clustering below diffraction detection limits cannot be fully excluded without higher-resolution techniques.

A simple mass balance shows that LPBF retains ~21–36% of the blended nitrogen (0.27–0.45 wt% retained vs. nominal 1.26 wt% in the feed), implying that ~0.8–1.0 wt% N is lost during processing. This loss likely arises to several concurrent mechanisms: (i) volatilization from the high-temperature melt pool, enhanced by recoil pressure; (ii) escape of gas bubbles formed as nitrogen is rejected during solidification; and (iii) rejection during δ-ferrite formation once its limited solubility is exceeded. Furthermore, because the build chamber atmosphere is argon rather than pressurized nitrogen, nitrogen replenishment at the melt pool surface is limited.

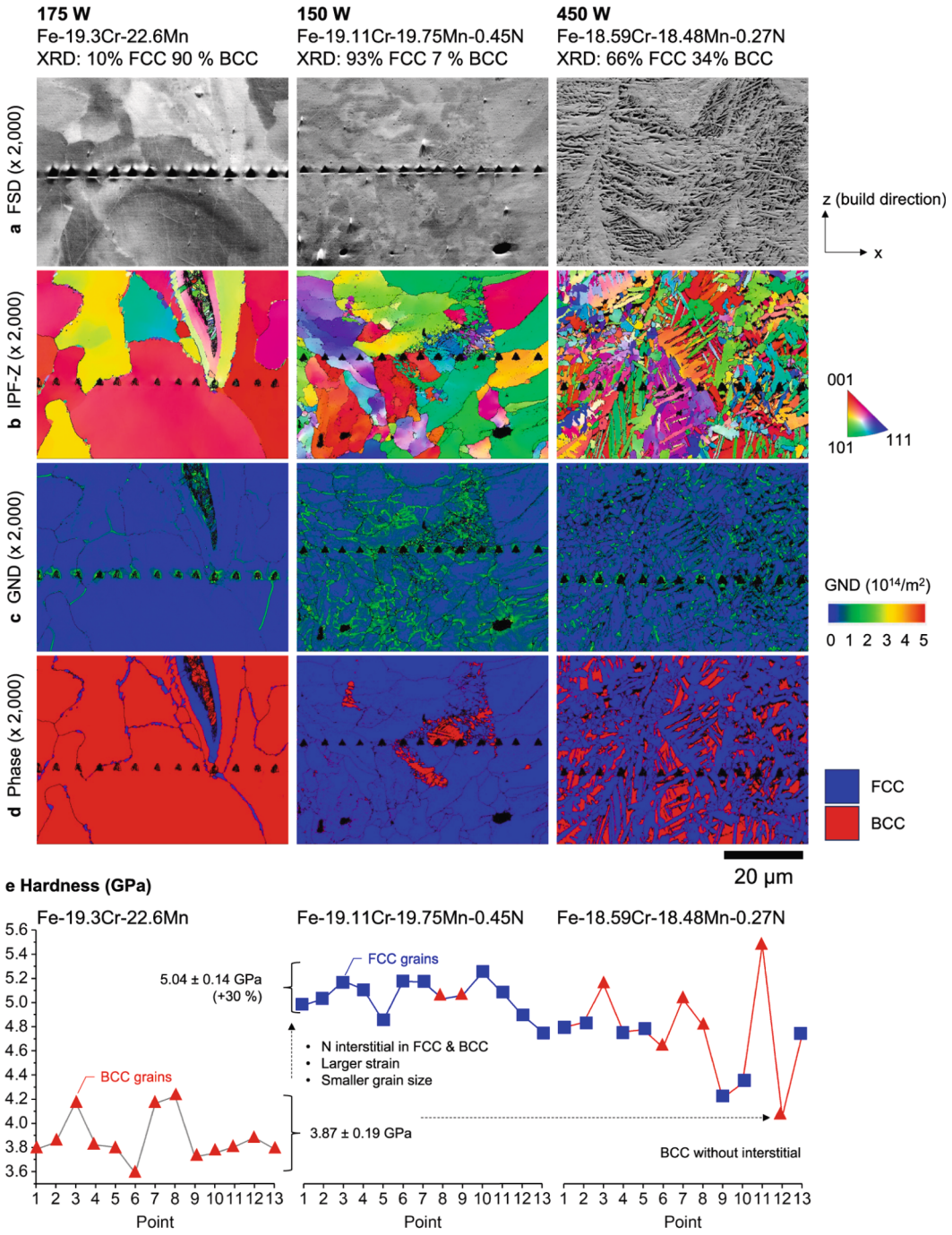

Fig. 6. Nanoindentation and EBSD characterization of LPBF-processed samples fabricated at different nitrogen contents. Shown are (a) forward-scattered electron (FSD) images, (b) inverse pole figure (IPF-Z) maps, (c) geometrically necessary dislocation (GND) density maps, (d) phase maps, and (e) nanoindentation hardness measured across γ-austenite (FCC) and δ-ferrite (BCC) regions.

Table 3
Mechanical and electrochemical performance of LPBF-processed nickel-free stainless steels fabricated under different conditions, together with reference alloys.

Method	Sample	Laser Power	Yield Strength	Ultimate Tensile Strength	Elongation	Corrosion Potential E_{corr}	Current Density I_{corr}	Pitting Potential	Pitting Current
		(W)	(MPa)	(MPa)	(%)	(mV)	(μA cm^{-2})	(mV)	(μA cm^{-2})
LPBF	Ni free, N free	175	498	604	15.0	–358 ± 30	2.5 ± 1.4	–	–
LPBF	Ni free, Cr-N	175	817 ± 6	969 ± 1	12.1 ± 1.5	–134 ± 11	0.2 ± 0.1	497 ± 69	6.8 ± 3.9
LPBF	SS316L	120	514 ± 12	605 ± 9	59.1 ± 3.5	–129 ± 9	0.1 ± 0.02	474 ± 116	0.5 ± 0.1
LPBF	SS304		–	–	–	–	–	495 ± 32	2.9 ± 0.2
Hot Rolled	Mild Steel	–	–	–	–	–689 ± 31	0.6 ± 0.4	–	–
LPBF	Ni free, Fe-N	450	882 ± 80	1062 ± 44	10.5 ± 4.3	–	–	–	–
LPBF	Ni free, Fe-N	150	744 ± 42	935 ± 57	20.8 ± 3.9	–400 ± 33	2.7 ± 1.4	–	–

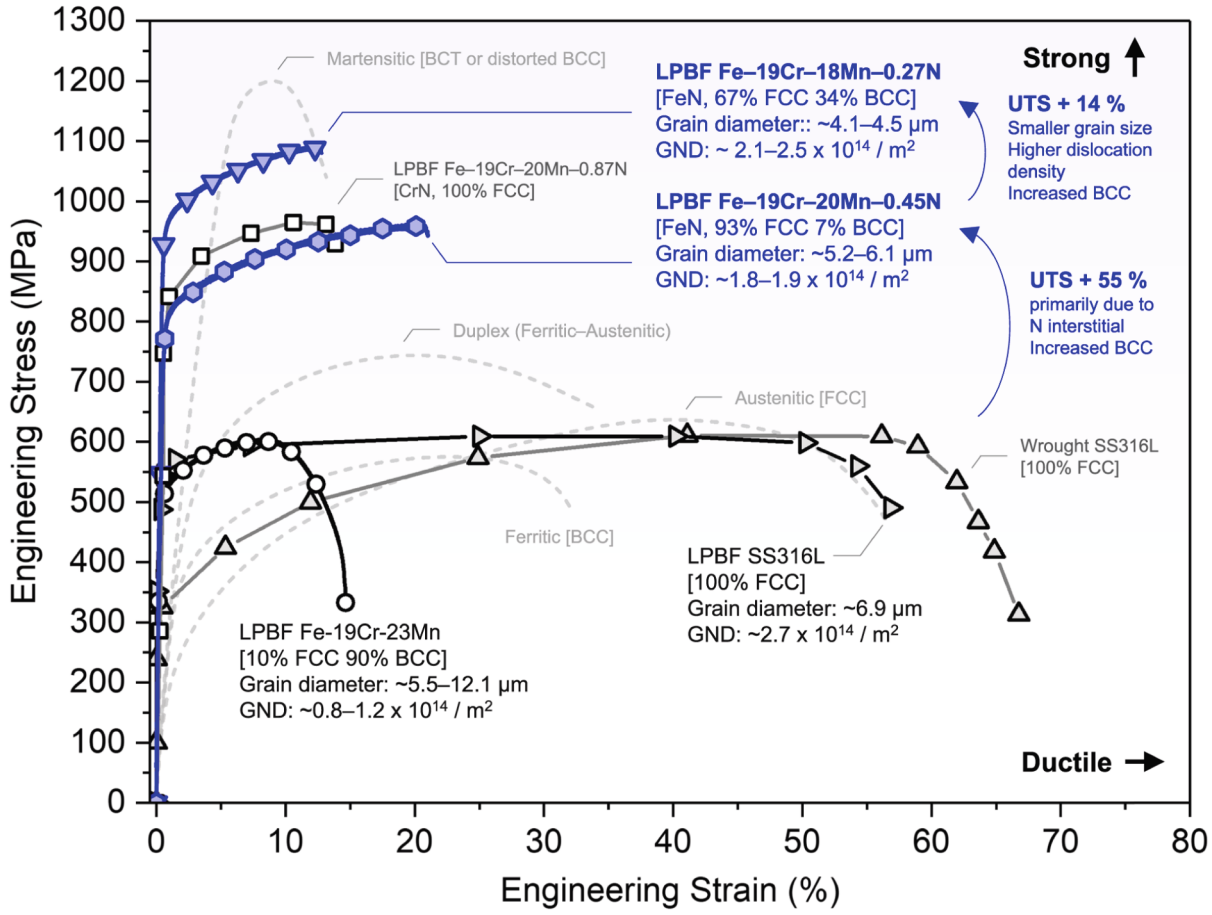

Fig. 7. Engineering stress–strain curves of LPBF-processed Fe–Cr–Mn–N alloys fabricated under different processing conditions, compared with nitrogen-free Fe–Cr–Mn steel, LPBF SS316L, and representative literature data [74,75].

Compared with higher decomposition temperature precursors such as Cr–N (~900 °C onset, **SI Fig. S12**), Fe–N offers a better kinetic match to LPBF's short thermal cycle, enabling nitrogen delivery without undissolved residues. However, the combination of volatilization and bubble escape caps retention below ~0.5 wt%, highlighting both the opportunity and current limitation of precursor-based nitrogen alloying under ambient-pressure LPBF.

4.2. Solidification path governs N retention and phase selection

In Ni-free, N-free Fe–19Cr–23Mn, solidification followed the path L → δ → δ + γ, producing coarse δ-ferrite grains with fine γ-austenite along prior boundaries (Fig. 6d). This matches the Fe–Cr–Mn–N phase map at 0 wt% N, where the absence of strong γ-austenite stabilizers biases primary δ-ferrite formation (Fig. 9, red arrow).

With Fe–N alloying, precursor decomposition and partial nitrogen uptake shift the composition trajectory toward γ-austenite stabilization. In the Fe–Cr–Mn–N phase map, three representative conditions can be identified (highlighted in Fig. 9):

Point 1: The observed depletion of Mn and N suggests that local melt-pool temperatures are sufficiently high to exceed the Fe melting point (~1500 °C) and, under certain processing conditions, may approach temperatures at which Mn volatilization becomes significant (boiling point ≈ 2061 °C), although peak temperatures were not measured directly.

Point 2: In both 150 W (~0.45 wt% N) and 450 W (~0.27 wt% N) builds, the microstructure consists of dual-phase γ-austenite and δ-ferrite. This corresponds to an initial L → δ solidification step, followed by entry into the two-phase δ + γ field during cooling.

Point 3: In contrast, Cr–N alloying (~0.87 wt% N) produced a fully γ-austenitic microstructure [68], consistent with a direct L → γ solidification path and subsequent stabilization entirely within the γ-austenite field.

Collectively, these observations indicate that nitrogen retention and manganese stability govern phase selection during LPBF, such that higher retained nitrogen favors γ-austenite stabilization, while increased volatilization at higher powers promotes δ-ferritic formation.

The presence of δ-ferrite in Fe–N alloys play a dual role: it restricts γ-austenite grain growth and promotes microstructural refinement (Fig. 5), but increasing δ-ferrite fraction reduces ductility and alters corrosion behavior (Table 3). Thus, the phase balance in Fe–N alloys is controlled by nitrogen retention and volatilization, which directly determine δ-ferrite fraction and thereby influence both microstructure and properties.

4.3. BCC phase indexed as δ-ferrite, instead of α′-martensite

Although the higher-power, mixed-phase condition reaches UTS ≈ 1.06 GPa (Fig. 7) — a strength often associated with martensitic steels. Multiple lines of evidence indicate that the observed BCC phase is δ-ferrite rather than α′-martensite.

First, thermodynamic estimates place the martensite-start

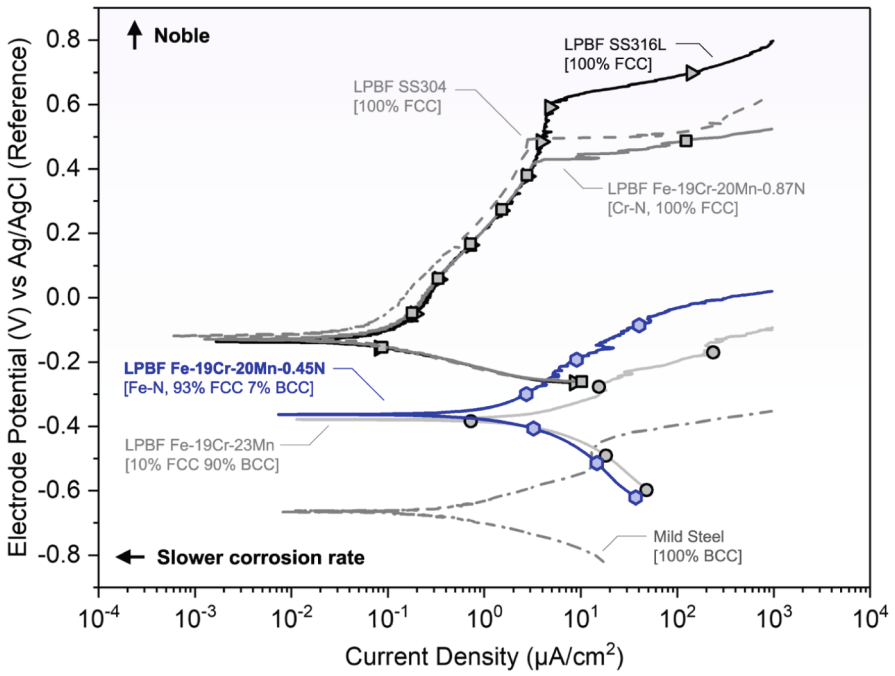

Fig. 8. Potentiodynamic polarization curves of LPBF-processed Fe–Cr–Mn–N alloys, nitrogen-free Fe–Cr–Mn steel, and reference alloys measured in 3.5 wt% NaCl using an Ag/AgCl (3 M KCl) reference electrode.

temperature (Ms) of the measured compositions below 0 °C (**SI Section S1**), making thermal $\gamma \rightarrow \alpha'$ transformation during cooling unlikely. Second, synchrotron and laboratory XRD detect only cubic BCC reflections, with no peak splitting indicative of body-centered tetragonal martensite; diffraction consistently identifies only γ-austenite (FCC) and δ-ferrite (BCC) (Fig. 3). Third, EBSD maps show thin BCC grains decorating prior melt-track and grain boundaries, lacking the clustered lath morphology or Kurdjumov–Sachs/Nishiyama–Wassermann orientation relationships characteristic of martensite (Figs. 5-6) [79].

This interpretation is further supported by compositional mapping. When projected onto a modified Schaeffler/DeLong diagram adjusted for high Mn and N contents (Fig. 10, **SI Table S6**), both 150 W and 450 W conditions fall within the γ + δ regions, well away from the martensite wedge. The low-power condition lies near the γ-austenite domain, while the higher-power state shifts deeper into γ + δ as Mn and N decrease — but neither approaches the martensite region. While Schaeffler-type maps are empirical and qualitative, particularly under LPBF's far-from-equilibrium cooling rates, the predicted trends are consistent with measured phase fractions and sub-zero Ms estimates.

Taken together, thermodynamic, diffraction, morphological, and map-level evidence converge on the conclusion that the BCC phase present in Fe–N builds originate from the solidification path (L → δ → δ + γ with partial δ retention), rather than from quenched martensitic formation.

4.4. *Strengthening mechanism and strength–ductility trade-off*

As shown in Section 3.4, γ-austenite rich conditions exhibit higher ductility at moderate strength, whereas δ-ferrite enriched states achieve higher strength at the expense of elongation (Fig. 7).

Strengthening of the Fe–N alloys arise from three concurrent mechanisms:

(i) interstitial solid-solution strengthening by nitrogen in γ-austenite,
(ii) grain refinement strengthening, and
(iii) dual-phase (γ/δ) strengthening.

These mechanisms operate across different length scales and are inherently coupled within the LPBF microstructure. Consequently, a strict additive or exact numerical partitioning of their individual contributions is not uniquely determinable from bulk tensile data alone. The following discussion therefore provides a mechanistically grounded, semi-quantitative assessment of their relative importance in differentiating strength among the present samples.

Interstitial nitrogen provides the baseline strengthening relative to the N-free reference alloy. This is evidenced by the systematic γ-austenite lattice expansion with increasing nitrogen content (Fig. 4c), the associated hardness increase (Fig. 4b), and the absence of detectable nitride precipitates within diffraction limits. Nitrogen therefore acts primarily as a solid-solution strengthener that elevates the overall strength level of the Fe–N system. However, among Fe–N samples processed at different laser powers, nitrogen content decreases from ~0.45 to ~0.27 wt%, while yield strength increases from 744 ± 42 MPa to 882 ± 80 MPa. This inverse trend indicates that interstitial nitrogen is not the dominant factor governing strength differences between processing conditions.

Grain refinement contributes a secondary strengthening effect. EBSD analysis shows that γ-austenite grain size decreases from ~17 μm to ~7 μm and δ-ferrite grain size from ~11 μm to ~6 μm with increasing laser power (Fig. 5, **SI Fig. S8**). Based on Hall–Petch scaling for austenitic steels, this refinement is expected to contribute on the order of several tens of MPa in yield strength. The accompanying increase in geometrically necessary dislocation density in γ-austenite reflects the development of LPBF-induced cellular dislocation substructures, further supporting a refinement-induced strengthening contribution. While significant, this effect alone cannot fully account for the observed strength increase.

Dual-phase (γ/δ) strengthening is therefore identified as the dominant factor governing strength differences among the present Fe–N samples. With increasing laser power, the δ-ferrite fraction increases from ~7% to ~33%, enhancing load partitioning and constraining

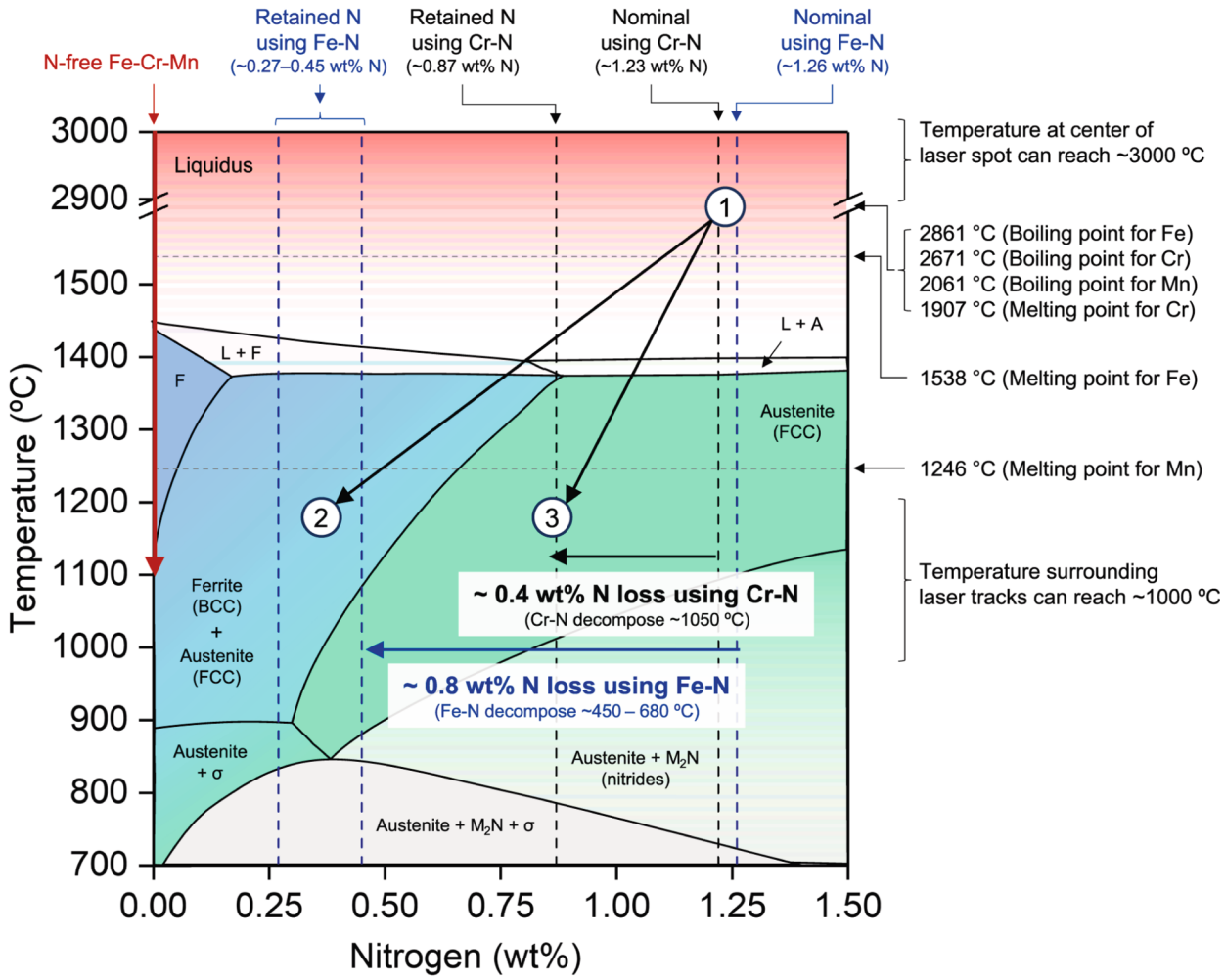

Fig. 9. Phase diagram of Fe–18Cr–18Mn–N system [52], with temperature plotted against nitrogen content and relevant phase fields indicated.

plastic flow, which leads to higher yield and ultimate tensile strengths [80]. Importantly, δ-ferrite forms in situ during LPBF along γ-austenite grain boundaries, producing metallurgically bonded γ/δ interfaces that enable effective load transfer and coordinated deformation between phases [81]. At lower δ-ferrite fractions, the softer γ-austenite phase accommodates plastic strain while the harder δ-ferrite phase provides constraint, contributing to the relatively high ductility observed in γ-rich microstructures. As the δ-ferrite fraction and γ/δ interface density increase, plastic deformation becomes increasingly localized within the γ-austenite phase, promoting earlier necking. Thus, while interfacial integrity is essential for coordinated deformation, the FCC/BCC phase ratio remains the primary factor controlling the strength–ductility balance in the present dual-phase Fe–N alloys.

4.5. Corrosion mechanisms and nitrogen's role in passivation

As presented in Section 3.5, Fe–N builds exhibit more noble corrosion potentials than the N-free baseline but remain intermediate between Cr–N assisted stainless steels and conventional SS316L (Fig. 8). This behavior reflects the coupled influence of retained nitrogen on both phase balance and passive film chemistry.

Interstitial nitrogen in γ-austenite enhances corrosion resistance through two complementary mechanisms. First, it stabilizes γ-austenite, thereby limiting the formation of δ-ferrite, which can otherwise act as preferential sites for localized corrosion. Second, nitrogen modifies the chemistry and defect structure of the passive film by promoting chromium enrichment and facilitating rapid repassivation. This interpretation is consistent with prior reports that nitrogen increases the donor density and conductivity of passive oxides [47,82]. The absence of detectable nitride precipitation within diffraction limit, as assessed by synchrotron diffraction, further supports this mechanism: retained nitrogen remains predominantly in interstitial solid-solution where it contributes directly to passivation rather than forming CrN, which would otherwise locally deplete chromium and weaken the protective film.

The comparatively lower corrosion resistance of Fe–N relative to Cr–N assisted alloys arises primarily from differences in achievable nitrogen content. With ~0.45 wt% retained nitrogen, Fe–N alloy exhibit measurable passivation enhancement, but this effect is less pronounced than in Cr–N routes where ~0.87 wt% N can be stabilized. Higher interstitial nitrogen contents strengthen passivation more effectively, leading to lower corrosion current densities. Similarly, the benchmark SS316L benefits from nickel-stabilized γ-austenite, which suppresses δ-ferrite formation and supports the development of a robust Cr-rich passive film, accounting for its superior corrosion resistance.

In addition to compositional effects, the spatial distribution of δ-ferrite contributes to the observed corrosion behavior. δ-ferrite differs electrochemically from γ-austenite and typically exhibits a more negative corrosion potential, establishing local micro-galvanic couples in which δ-ferrite acts as the anodic phase and γ-austenite as the cathodic

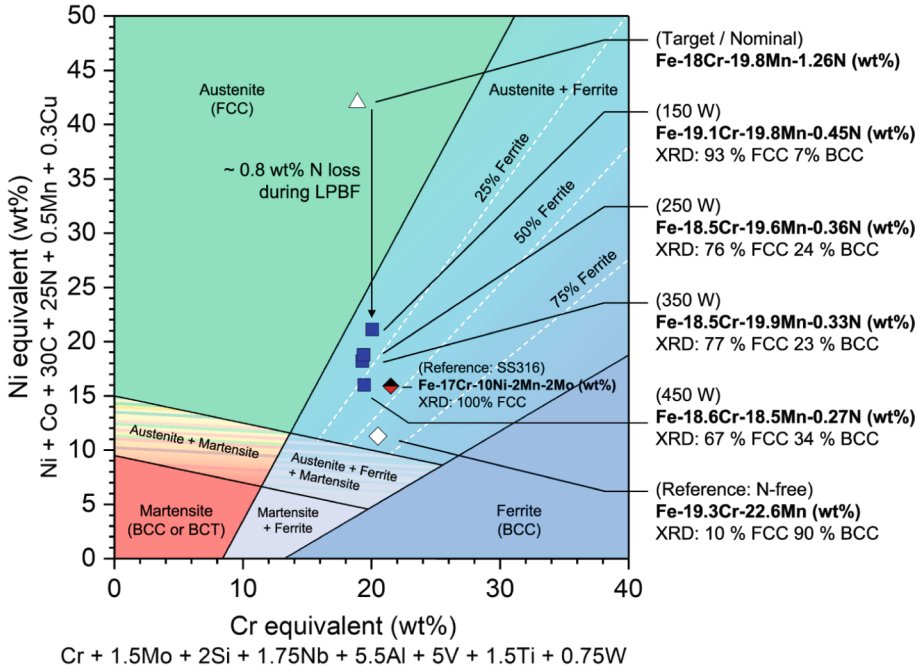

Fig. 10. Revised Schaeffler's diagram showing predicted phase regions as a function of chromium and nickel equivalents, with experimentally measured compositions of LPBF-processed alloys overlaid.

phase under chloride exposure [83,84]. Moreover, δ-ferrite has a much lower nitrogen solubility, resulting in locally nitrogen-depleted regions with thinner, less chromium-enriched passive films and reduced repassivation kinetics [85]. Partitioning of alloying elements across γ/δ interfaces further introduces local chemical heterogeneity, making these regions preferential sites for passive film breakdown and pit initiation. While minor δ fractions refine the microstructure and enhance mechanical strength, their electrochemical activity can promote localized corrosion [86].

Taken together, these findings support the conclusion that nitrogen plays a dual role in corrosion protection of nickel-free stainless steels: it stabilizes γ-austenite to suppress δ-ferrite formation and enhances passive film stability through interstitial solid-solution. Maximizing these benefits depends on achieving higher nitrogen retention, which remains the limiting factor for Fe–N route compared to Cr–N assisted alloying under the present LPBF conditions.

4.6. *Trade-off between mechanical performance and corrosion resistance*

The present results highlight a systematic trade-off between mechanical strengthening and corrosion performance in LPBF-fabricated Fe–N stainless steels. As shown in Table 3 and Fig. 7, increasing δ-ferrite fraction with laser power leads to higher strength, accompanied by reductions in ductility and corrosion resistance performance. For example, the γ-austenite rich condition at 150 W (~93% γ, ~0.45 wt% N) exhibits a yield strength of 744 ± 42 MPa with 20.8 ± 3.9% elongation, whereas the δ-ferrite enriched condition at 450 W (~33% δ, ~0.27 wt% N) attains a higher yield strength of 882 ± 80 MPa but reduced ductility (10.5 ± 4.3%).

This mechanical enhancement is accompanied by changes in corrosion response. As shown in Table 3 and Fig. 8, the γ-austenite rich Fe–N condition exhibits a corrosion potential of –400 ± 33 mV in 3.5 wt% NaCl, compared with –358 ± 30 mV for the N-free baseline and –134 ± 11 mV for the Cr–N alloyed reference. While the Fe–N alloys do not achieve the corrosion resistance of Cr–N or Ni-containing stainless steels, nitrogen addition nevertheless modifies passivation behavior relative to fully nitrogen-free alloys, as discussed in Section 4.5.

This trade-off arises from the dual role of δ-ferrite. Mechanically, increasing δ-ferrite content and γ/δ interface density enhances load partitioning and constrains plastic deformation, thereby increasing strength. Electrochemically, δ-ferrite introduces local chemical and electrochemical heterogeneity that promotes micro-galvanic coupling and passive film instability at δ-rich regions (Section 4.5). Importantly, this behavior defines a tunable design space rather than a fundamental limitation, allowing LPBF processing parameters to be selected according to application-specific priorities, such as maximizing strength or balancing ductility and corrosion resistance.

5. Conclusions

This study demonstrates a viable approach for producing nickel-free, nitrogen-alloyed stainless steels by laser powder bed fusion (LPBF) using Fe–N as a low-temperature nitrogen source. The key conclusions are as follows:

1. Fe–N decomposes at ~450–680 °C, enabling LPBF builds with near-full density (>99.5%) and interstitial nitrogen retention of ~0.27–0.45 wt%. No secondary nitrides were detected within diffraction limits, indicating that retained nitrogen predominantly accommodated in interstitial solid-solution.
2. At a scan speed of 500 mm s^{-1}, hatch spacing of 0.1 mm, layer thickness of 0.03 mm and laser spot size of 0.1 mm, low laser power (150 W) maximized nitrogen retention (~0.45 wt%), producing ~93% γ-austenite (FCC) and ~7% δ-ferrite (BCC). Increasing laser power (450 W) reduced nitrogen retention to ~0.27 wt%, yielding ~67% γ-austenite and 33% δ-ferrite.
3. Interstitial nitrogen provides the baseline strengthening relative to nitrogen-free alloys, while γ-austenite / δ-ferrite balance governs strength-ductility trade-offs across processing conditions. Relative to the Ni-free, N-free baseline, hardness increased from 266 HV to 326 HV (~25%) and nanoindentation from 3.89 GPa to 5.04 GPa (~30%). Tensile properties ranged from YS ≈ 744 MPa, UTS ≈ 935

MPa, El ≈ 21% (γ-rich, ~0.45 wt% N) to YS ≈ 882 MPa, UTS ≈ 1062 MPa, El ≈ 10.5% (δ-rich, ~0.27 wt% N).

4. Nitrogen addition modified corrosion behavior relative to the Ni-free, N-free baseline in 3.5 wt% NaCl, although the extracted corrosion current density remained elevated. Overall corrosion performance remained below that of Cr–N-alloyed steels and conventional SS316L, reflecting limitations in achievable nitrogen retention and the presence of δ-ferrite.

By demonstrating that interstitial nitrogen can be delivered and partially retained during LPBF without high-pressure apparatus or detectable nitride precipitation, this work provides a foundation for designing next-generation nickel-free stainless steels. The ability to tune γ-austenite / δ-ferrite phase balance, strength–ductility response, and corrosion resistance through process control positions Fe–N alloying as a promising platform for future optimization toward biomedical, structural, and energy-related applications.

CRediT authorship contribution statement

Wei Hock Teh: Writing – original draft, Formal analysis, Data curation. **Jing Jun Lee:** Methodology, Investigation, Formal analysis. **Li Tian Chew:** Methodology, Investigation, Formal analysis. **Kok Heng Cheong:** Methodology, Investigation, Formal analysis. **Yakai Zhao:** Methodology, Investigation, Formal analysis. **Baisong Cheng:** Writing – review & editing, Validation, Supervision, Formal analysis, Conceptualization. **Fengxia Wei:** Writing – review & editing, Validation, Supervision, Formal analysis, Conceptualization. **Tim J. White:** Writing – review & editing, Validation, Supervision. **Cheng Cheh Tan:** Writing – review & editing, Validation, Supervision, Formal analysis, Conceptualization.

Declaration of competing interest

The authors declare that they have no known competing financial interests or personal relationships that could have appeared to influence the work reported in this paper.

Acknowledgment

This work was supported by The Agency for Science, Technology and Research (A*STAR) under its RIE2025 Manufacturing, Trade and Connectivity (MTC) Industry Alignment Fund Pre-positioning (IAF-PP) Grant (Award M24N2a0041), Closed-Loop Advanced Manufacturing Processes (c-LAMP) programme, and Singapore-International Synchrotron Access Programme (SG-ISAP) beamtime at the Australian Synchrotron, part of the Australian Nuclear Science and Technology Organization (ANSTO). We would like to thank Dr Gu Qinfen, Dr. Anita D'Angelo, beamline scientist at ANSTO who assisted in the beamline experiment.

Appendix A. Supplementary data

Supplementary data to this article can be found online at https://doi.org/10.1016/j.matdes.2026.115719.

Data availability

Data will be made available on request.

References

[1] L. Gardner, The use of stainless steel in structures, Prog. Struct. Eng. Mater. 7 (2) (2005) 45–55, https://doi.org/10.1002/pse.190.
[2] N.R. Baddoo, Stainless steel in construction: a review of research, applications, challenges and opportunities, J. Constr. Steel Res. 64 (11) (2008) 1199–1206, https://doi.org/10.1016/j.jcsr.2008.07.011.
[3] S. Fashu, V. Trabadelo, A critical review on development, performance and selection of stainless steels and nickel alloys for the wet phosphoric acid process, Mater. Des. 227 (2023) 111739, https://doi.org/10.1016/j.matdes.2023.111739.
[4] A. Panagopoulos, M. Loizidou, K.-J. Haralambous, Stainless steel in thermal desalination and brine treatment: current status and prospects, Met. Mater. Int. 26 (10) (2020) 1463–1482, https://doi.org/10.1007/s12540-019-00398-w.
[5] M. Dundu, Evolution of stress–strain models of stainless steel in structural engineering applications, Constr. Build. Mater. 165 (2018) 413–423, https://doi.org/10.1016/j.conbuildmat.2018.01.008.
[6] G. Chai and P. Kangas, Recent Developments of Advanced Austenitic and Duplex Stainless Steels for Oil and Gas Industry, in Energy Materials 2014, 2016, Cham: Springer International Publishing, DOI: https://doi.org/10.1007/978-3-319-48765-6_85.
[7] M. Saravanan, A. Devaraju, N. Venkateshwaran, A. Krishnakumari, and J. Saarvesh, A review on recent progress in coatings on AISI austenitic stainless steel, Materials Today: Proceedings, 2018, 5(6, Part 2): p. 14392-14396, DOI: https://doi.org/10.1016/j.matpr.2018.03.024.
[8] G. Meric de Bellefon, J.C. van Duysen, Tailoring plasticity of austenitic stainless steels for nuclear applications: Review of mechanisms controlling plasticity of austenitic steels below 400 °C, J. Nucl. Mater. 475 (2016) 168–191, https://doi.org/10.1016/j.jnucmat.2016.04.015.
[9] U. Ehrnstén, P.L. Andresen, Z. Que, A review of stress corrosion cracking of austenitic stainless steels in PWR primary water, J. Nucl. Mater. 588 (2024) 154815, https://doi.org/10.1016/j.jnucmat.2023.154815.
[10] A. Kohyama, M.L. Grossbeck, G. Piatti, The application of austenitic stainless steels in advanced fusion systems: current limitations and future prospects, J. Nucl. Mater. 191–194 (1992) 37–44, https://doi.org/10.1016/S0022-3115(09)80008-1.
[11] K. Yang, Y. Ren, Nickel-free austenitic stainless steels for medical applications, Sci. Technol. Adv. Mater. 11 (1) (2010) 014105, https://doi.org/10.1088/1468-6996/11/1/014105.
[12] M. Sumita, T. Hanawa, S.H. Teoh, Development of nitrogen-containing nickel-free austenitic stainless steels for metallic biomaterials—review, Mater. Sci. Eng. C 24 (6) (2004) 753–760, https://doi.org/10.1016/j.msec.2004.08.030.
[13] M. Talha, Y. Ma, Y. Lin, Y. Pan, X. Kong, O. P. Sinha, and C. K. Behera, Corrosion performance of cold deformed austenitic stainless steels for biomedical applications, 2019, 37(4): p. 283-306, DOI: https://doi.org/10.1515/corrrev-2019-0004.
[14] Y. Xu, Y. Li, T. Chen, C. Dong, K. Zhang, X. Bao, A short review of medical-grade stainless steel: Corrosion resistance and novel techniques, J. Mater. Res. Technol. 29 (2024) 2788–2798, https://doi.org/10.1016/j.jmrt.2024.01.240.
[15] D. Giuliodori, A. Rodriguez, Analysis of the stainless steel market in the EU, China and US using co-integration and VECM, Resour. Policy 44 (2015) 12–24, https://doi.org/10.1016/j.resourpol.2014.11.006.
[16] I. Baker, Stainless Steel, in Fifty Materials That Make the World, I. Baker, 2018, Springer International Publishing: Cham. p. 223-228, DOI: https://doi.org/10.1007/978-3-319-78766-4_42.
[17] L.P. Karjalainen, T. Taulavuori, M. Sellman, A. Kyröläinen, Some strengthening methods for austenitic stainless steels, Steel Res. Int. 79 (6) (2008) 404–412, https://doi.org/10.1002/srin.200806146.
[18] R.-B. Song, J.-Y. Xiang, D.-P. Hou, Characteristics of mechanical properties and microstructure for 316L austenitic stainless steel, J. Iron Steel Res. Int. 18 (11) (2011) 53–59, https://doi.org/10.1016/S1006-706X(11)60117-9.
[19] R.K. Desu, H. Nitin Krishnamurthy, A. Balu, A.K. Gupta, S.K. Singh, Mechanical properties of Austenitic Stainless Steel 304L and 316L at elevated temperatures, J. Mater. Res. Technol. 5 (1) (2016) 13–20, https://doi.org/10.1016/j.jmrt.2015.04.001.
[20] L. Zhang, M. Wen, M. Imade, S. Fukuyama, K. Yokogawa, Effect of nickel equivalent on hydrogen gas embrittlement of austenitic stainless steels based on type 316 at low temperatures, Acta Mater. 56 (14) (2008) 3414–3421, https://doi.org/10.1016/j.actamat.2008.03.022.
[21] N. Campagnol, K. Hoffman, A. Lala, O. Ramsbottom, The Future of Nickel: A Class Act, McKinsey & Company, Basic Materials, 2017.
[22] A.H. Olafsdottir, H.U. Sverdrup, Modelling global nickel mining, supply, recycling, stocks-in-use and price under different resources and demand assumptions for 1850–2200, Min. Metall. Explor. 38 (2) (2021) 819–840, https://doi.org/10.1007/s42461-020-00370-y.
[23] J. Menzel, W. Kirschner, G. Stein, High nitrogen containing Ni-free austenitic steels for medical applications, ISIJ Int. 36 (7) (1996) 893–900, https://doi.org/10.2355/isijinternational.36.893.
[24] W. Bal, H. Kozłowski, K.S. Kasprzak, Molecular models in nickel carcinogenesis, J. Inorg. Biochem. 79 (1–4) (2000) 213–218, https://doi.org/10.1016/s0162-0134(99)00169-5.
[25] J.C. Wataha, N.L. O'Dell, B.B. Singh, M. Ghazi, G.M. Whitford, P.E. Lockwood, Relating nickel-induced tissue inflammation to nickel release in vivo, J. Biomed. Mater. Res. 58 (5) (2001) 537–544, https://doi.org/10.1002/jbm.1052.
[26] S. Şahin, M. Übeyli, A review on the potential use of austenitic stainless steels in nuclear fusion reactors, J. Fusion Energ. 27 (4) (2008) 271–277, https://doi.org/10.1007/s10894-008-9136-3.
[27] Y.-P. Lang, H.-P. Qu, H.-T. Chen, Y.-Q. Weng, Research progress and development tendency of nitrogen-alloyed austenitic stainless steels, J. Iron Steel Res. Int. 22 (2) (2015) 91–98, https://doi.org/10.1016/S1006-706X(15)60015-2.
[28] S. Li, C. Zhang, J. Lu, R. Chen, D. Chen, G. Cui, A review of progress on high nitrogen austenitic stainless-steel research, Mater. Express 11 (12) (2021) 1901–1925, https://doi.org/10.1166/mex.2021.2109.

[29] Y.H. Kim, K.Y. Kim, Y.D. Lee, Nitrogen-alloyed, metastable austenitic stainless steel for automotive structural applications, Mater. Manuf. Process. 19 (1) (2004) 51–59, https://doi.org/10.1081/AMP-120027498.

[30] E. Salahinejad, R. Amini, M.J. Hadianfard, Structural evolution during mechanical alloying of stainless steels under nitrogen, Powder Technol. 215–216 (2012) 247–253, https://doi.org/10.1016/j.powtec.2011.10.012.

[31] L. Patnaik, S. Ranjan Maity, and S. Kumar, Status of nickel free stainless steel in biomedical field: A review of last 10 years and what else can be done, Materials Today: Proceedings, 2020, 26: p. 638-643, DOI: https://doi.org/10.1016/j.matpr.2019.12.205.

[32] M.O. Speidel, Nitrogen Containing Austenitic Stainless Steels, Mater. Werkst. 37 (10) (2006) 875–880, https://doi.org/10.1002/mawe.200600068.

[33] R.P. Reed, Nitrogen in austenitic stainless steels, JOM 41 (1989) 16–21, https://doi.org/10.1007/BF03220991.

[34] M. Talha, C.K. Behera, O.P. Sinha, A review on nickel-free nitrogen containing austenitic stainless steels for biomedical applications, Mater. Sci. Eng. C 33 (7) (2013) 3563–3575, https://doi.org/10.1016/j.msec.2013.06.002.

[35] H. Baba, T. Kodama, Y. Katada, Role of nitrogen on the corrosion behavior of austenitic stainless steels, Corros. Sci. 44 (10) (2002) 2393–2407, https://doi.org/10.1016/S0010-938X(02)00040-9.

[36] P. Müllner, C. Solenthaler, P. Uggowitzer, M. Speidel, On the effect of nitrogen on the dislocation structure of austenitic stainless steel, Mater. Sci. Eng. A 164 (1–2) (1993) 164–169, https://doi.org/10.1016/0921-5093(93)90655-X.

[37] Y. Cho, H.-J. Cho, H.-S. Noh, S.-H. Kim, S.-J. Kim, Strengthening mechanism and martensite transformation behavior in grain-refined low-Ni austenitic stainless steel, Mater. Sci. Eng. A 916 (2024) 147368, https://doi.org/10.1016/j.msea.2024.147368.

[38] S.P. Ambade, C.K. Tembhurkar, A. Patil, A.V. Tidke, S.D. Shelare, C. Prakash, M. B. Djukic, N. Khosravi, P. Paramasivam, Microstructure, mechanical properties and sensitization of ultra-low nickel Cr–Mn austenitic stainless steels, J. Mater. Res. Technol. 30 (2024) 4353–4365, https://doi.org/10.1016/j.jmrt.2024.04.127.

[39] V.H. Mafra Monfredo Ferreira, F.G. Coury, D. de Araujo Santana, G.Y. Koga, Novel high nitrogen austenitic stainless steels: from high-throughput screening to experimental validation and properties relationship, J. Mater. Res. Technol. 30 (2024) 640–656, https://doi.org/10.1016/j.jmrt.2024.03.090.

[40] H.-J. Cho, Y. Cho, H. Gwon, S. Lee, S.S. Sohn, S.-J. Kim, Effects of Ni/Cu replacement on improvement of tensile and hydrogen-embrittlement properties in austenitic stainless steels, Acta Mater. 235 (2022) 118093, https://doi.org/10.1016/j.actamat.2022.118093.

[41] A. Di Schino, M. Barteri, J.M. Kenny, Effects of grain size on the properties of a low nickel austenitic stainless steel, J. Mater. Sci. 38 (23) (2003) 4725–4733, https://doi.org/10.1023/A:1027470917858.

[42] P. Pistorius and M. Du Toit, Low-nickel austenitic stainless steels: metallurgical constraints, in 12th Int. Ferroalloys Congress, held June, 2010.

[43] R. Zhou, D.O. Northwood, C. Liu, On nitrogen diffusion during solution treatment in a high nitrogen austenitic stainless steel, J. Mater. Res. Technol. 9 (2) (2020) 2331–2337, https://doi.org/10.1016/j.jmrt.2019.12.064.

[44] R. Dhanasekar, T. Satish Kumar, K. Krishna Kumar, N. Jeyaprakash, Physical simulation of the heat-affected zone in nickel-free high-nitrogen stainless steel weld at various peak temperatures and cooling rates, Mater. Today Commun. 38 (2024) 107996, https://doi.org/10.1016/j.mtcomm.2023.107996.

[45] V.G. Gavriljuk, Nitrogen in iron and steel, ISIJ Int. 36 (7) (1996) 738–745, https://doi.org/10.2355/isijinternational.36.738.

[46] C.-O.-A. Olsson, The influence of nitrogen and molybdenum on passive films formed on the austenoferritic stainless steel 2205 studied by AES and XPS, Corros. Sci. 37 (3) (1995) 467–479, https://doi.org/10.1016/0010-938X(94)00148-Y.

[47] G. Hj, The role of nitrogen in the corrosion of iron and steels, ISIJ Int. 36 (7) (1996) 777–786, https://doi.org/10.2355/isijinternational.36.777.

[48] I. Olefjord, L. Wegrelius, The influence of nitrogen on the passivation of stainless steels, Corros. Sci. 38 (7) (1996) 1203–1220, https://doi.org/10.1016/0010-938X(96)00018-2.

[49] D. Senk, K. Christmann, S. Geimer, D. Rzehak, Nitrogen solubility in high-manganese steel grades, Steel Res. Int. 87 (1) (2016) 107–111, https://doi.org/10.1002/srin.201400557.

[50] Z. Jiang, H. Li, Z. Chen, Z. Huang, D. Zou, L. Liang, The nitrogen solubility in molten stainless steel, Steel Res. Int. 76 (10) (2005) 740–745, https://doi.org/10.1002/srin.200506090.

[51] F. Takahashi, Y. Momoi, K. Kajikawa, H. Yamada, Effect of nitrogen content on cold working properties of high-strength Mn–Cr–N steels made using pressurized ESR, ISIJ Int. 55 (3) (2015) 578–585, https://doi.org/10.2355/isijinternational.55.578.

[52] C. Qiu, Thermodynamic analysis and evaluation of the Fe-Cr-Mn-N system, Metall. Trans. A 24 (11) (1993) 2393–2409, https://doi.org/10.1007/BF02646519.

[53] S.R. Narasimharaju, W. Zeng, T.L. See, Z. Zhu, P. Scott, X. Jiang, S. Lou, A comprehensive review on laser powder bed fusion of steels: processing, microstructure, defects and control methods, mechanical properties, current challenges and future trends, J. Manuf. Process. 75 (2022) 375–414, https://doi.org/10.1016/j.jmapro.2021.12.033.

[54] A. Antikainen, T. Jokiaho, J. Lagerbom, T. Lindroos, Nitrogen alloyed austenitic Ni-free stainless steel for additive manufacturing, Powder Metall. 67 (2–3) (2024) 98–109, https://doi.org/10.1177/00325899241248996.

[55] J. Boes, A. Röttger, W. Theisen, Microstructure and properties of high-strength C + N austenitic stainless steel processed by laser powder bed fusion, Addit. Manuf. 32 (2020) 101081, https://doi.org/10.1016/j.addma.2020.101081.

[56] L.A. Tochiro, A.H.G. Gabriel, M. Terada, R.S. de Castro, É.S.N. Lopes, J.A. Avila, M. Masoumi, Powder bed fusion of high-Mn-N Ni-free austenitic stainless steel: achieving low porosity and high mechanical strength through process parameter selection, Int. J. Adv. Manuf. Technol. 131 (3) (2024) 1377–1396, https://doi.org/10.1007/s00170-024-13073-1.

[57] L. Wang, X. Zhang, Y. Li, Z. Chen, H. Li, Y. Peng, D. Yang, K. Wang, Microstructures and mechanical properties of powder-filled laser welding joints composed of high-nitrogen steel, J. Mater. Res. Technol. 26 (2023) 2907–2918, https://doi.org/10.1016/j.jmrt.2023.08.115.

[58] K. Yang, M. Chen, K. Zhao, Z. Jia, Z. Wang, H. Qi, G. Sun, Research on gas pore formation and inhibition mechanism of high nitrogen steel during laser direct metal deposition, Opt. Laser Technol. 175 (2024) 110788, https://doi.org/10.1016/j.optlastec.2024.110788.

[59] A. Arabi-Hashemi, X. Maeder, R. Figi, C. Schreiner, S. Griffiths, C. Leinenbach, 3D magnetic patterning in additive manufacturing via site-specific in-situ alloy modification, Appl. Mater. Today 18 (2020) 100512, https://doi.org/10.1016/j.apmt.2019.100512.

[60] D. Yang, Y. Huang, J. Fan, M. Jin, Y. Peng, K. Wang, Effect of N2 content in shielding gas on formation quality and microstructure of high nitrogen austenitic stainless steel fabricated by wire and arc additive manufacturing, J. Manuf. Process. 61 (2021) 261–269, https://doi.org/10.1016/j.jmapro.2020.11.020.

[61] S. Astafurov, E. Astafurova, K. Reunova, E. Melnikov, M. Panchenko, V. Moskvina, G. Maier, V. Rubtsov, E. Kolubaev, Electron-beam additive manufacturing of high-nitrogen steel: Microstructure and tensile properties, Mater. Sci. Eng. A 826 (2021) 141951, https://doi.org/10.1016/j.msea.2021.141951.

[62] X. Zhang, Q. Zhou, K. Wang, Y. Peng, J. Ding, J. Kong, S. Williams, Study on microstructure and tensile properties of high nitrogen Cr-Mn steel processed by CMT wire and arc additive manufacturing, Mater. Des. 166 (2019) 107611, https://doi.org/10.1016/j.matdes.2019.107611.

[63] M. Qian, S. Song, Z. Yang, Y. Guo, K. Wang, A comparison of wire-feed additive manufacturing and hybrid additive/subtractive manufacturing of high nitrogen steel, J. Mater. Res. Technol. 33 (2024) 4092–4104, https://doi.org/10.1016/j.jmrt.2024.10.090.

[64] T. Wu, J. Liu, K. Wang, L. Wang, X. Zhang, Microstructure and mechanical properties of wire-powder hybrid additive manufacturing for high nitrogen steel, J. Manuf. Process. 70 (2021) 248–258, https://doi.org/10.1016/j.jmapro.2021.08.029.

[65] D. Yang, H. Fang, Y. Peng, J. Fan, Y. Huang, K. Wang, D. Yan, D. Li, Investigation of spatters in cold metal transfer + pulse-based wire and arc additive manufacturing of high nitrogen austenitic stainless steel, J. Mater. Eng. Perform. 30 (9) (2021) 6881–6894, https://doi.org/10.1007/s11665-021-06048-w.

[66] X. Zhang, Q. Zhao, C. Liu, Y. Peng, Y. Huang, J. Kong, K. Wang, On the formation of oxide inclusions in the high nitrogen chromium-manganese steel produced by the Wire and Arc Additive Manufacturing, J. Mater. Res. Technol. 33 (2024) 3852–3863, https://doi.org/10.1016/j.jmrt.2024.10.103.

[67] L. Becker, F. Radtke, J. Lentz, S. Benito, C. Broeckmann, S. Weber, Powder metallurgy and additive manufacturing of high-nitrogen alloyed FeCr(Si)N stainless steel, Adv. Eng. Mater. n/a(n/a) (2024) 2402293, https://doi.org/10.1002/adem.202402293.

[68] B. Cheng, F. Wei, W.H. Teh, J.J. Lee, T.L. Meng, K.B. Lau, L.T. Chew, Z. Zhang, K. H. Cheong, C.K. Ng, P. Wang, C.C. Tan, U. Ramamurty, Ambient pressure fabrication of Ni-free high nitrogen austenitic stainless steel using laser powder bed fusion method, Addit. Manuf. 55 (2022) 102810, https://doi.org/10.1016/j.addma.2022.102810.

[69] C. König, E. H. Valente, V. K. Nadimpalli, Y. G. Tokman, T. L. Christiansen, and M. A. J. Somers, Nickel-free austenitic stainless steel manufactured by laser powder-bed fusion from martensitic powder mixed with interstitial compounds, 2024, 79 (6): p. 269-287, DOI: https://doi.org/10.1515/htm-2024-0026.

[70] H.A. Wriedt, N.A. Gokcen, R.H. Nafziger, The Fe-N (Iron-nitrogen) system, Bull. Alloy Phase Diagr. 8 (4) (1987) 355–377, https://doi.org/10.1007/BF02869273.

[71] C.F. Holder, R.E. Schaak, Tutorial on powder X-ray diffraction for characterizing nanoscale materials, ACS Nano 13 (7) (2019) 7359–7365, https://doi.org/10.1021/acsnano.9b05157.

[72] H. Khan, A.S. Yerramilli, A. D'Oliveira, T.L. Alford, D.C. Boffito, G.S. Patience, Experimental methods in chemical engineering: X-ray diffraction spectroscopy—XRD, Can. J. Chem. Eng. 98 (6) (2020) 1255–1266, https://doi.org/10.1002/cjce.23747.

[73] F. Wei, B. Cheng, P. Kumar, P. Wang, J.J. Lee, H.L. Seng, K.H. Cheong, K.B. Lau, C. C. Tan, A comparative study of additive manufactured and wrought SS316L: Pre-existing dislocations and grain boundary characteristics, Mater. Sci. Eng. A 833 (2022) 142546, https://doi.org/10.1016/j.msea.2021.142546.

[74] I. Arrayago, E. Real, L. Gardner, Description of stress–strain curves for stainless steel alloys, Mater. Des. 87 (2015) 540–552, https://doi.org/10.1016/j.matdes.2015.08.001.

[75] S.K. Basantia, A. Bhattacharya, N. Khutia, D. Das, Plastic behavior of ferrite–pearlite, ferrite–bainite and ferrite–martensite steels: experiments and micromechanical modelling, Met. Mater. Int. 27 (5) (2021) 1025–1043, https://doi.org/10.1007/s12540-019-00519-5.

[76] P.A. Hooper, Melt pool temperature and cooling rates in laser powder bed fusion, Addit. Manuf. 22 (2018) 548–559, https://doi.org/10.1016/j.addma.2018.05.032.

[77] B. Lane, S. Moylan, E.P. Whitenton, L. Ma, Thermographic measurements of the commercial laser powder bed fusion process at NIST, Rapid Prototyp. J. 22 (5) (2016) 778–787, https://doi.org/10.1108/rpj-11-2015-0161.

[78] U.R. Lenel, B.R. Knott, Microstructure-composition relationships and Ms temperatures in Fe-Cr-Mn-N alloys, Metall. Trans. A 18 (5) (1987) 767–775, https://doi.org/10.1007/BF02646919.

[79] X.Y. He, Z.P. Xu, G.S. Rohrer, C. Kong, S. Primig, N. Haghdadi, Effect of template δ-ferrite microstructures on the ferrite-to-austenite phase transformation and

interphase boundary character distributions in additively manufactured duplex stainless steels, Materialia 43 (2025) 102509, https://doi.org/10.1016/j.mtla.2025.102509.
[80] W. Zhao, H. Xiang, X. Zhan, X. Zhang, C. Wu, In-situ EBSD study of the coordinated deformation behavior of 2205 duplex stainless steel fabricated via laser powder bed fusion during the tensile process, Mater. Sci. Eng. A 901 (2024) 146572, https://doi.org/10.1016/j.msea.2024.146572.
[81] A. Mateo, L. Llanes, L. Iturgoyen, M. Anglada, Cyclic stress-strain response and dislocation substructure evolution of a ferrite-austenite stainless steel, Acta Mater. 44 (3) (1996) 1143–1153, https://doi.org/10.1016/1359-6454(95)00197-2.
[82] F. Gao, Y. Qiao, J. Chen, L. Yang, H. Zhou, Z. Zheng, L. Zhang, Effect of nitrogen content on corrosion behavior of high-nitrogen austenitic stainless steel, npj Mater. Degrad. 7 (1) (2023) 75, https://doi.org/10.1038/s41529-023-00394-x.
[83] G. Obulan Subramanian, B.S. Kong, H.J. Lee, C. Jang, Evaluation of the thermal aging of δ-ferrite in austenitic stainless steel welds by electrochemical analysis, Sci. Rep. 8 (1) (2018) 15091, https://doi.org/10.1038/s41598-018-33422-x.
[84] J. Moon, H.-Y. Ha, T.-H. Lee, C. Lee, Different aspect of pitting corrosion and interphase corrosion in the weld heat-affected zone of high-nitrogen Fe–18Cr–10Mn–N steel, Mater. Chem. Phys. 142 (2) (2013) 556–563, https://doi.org/10.1016/j.matchemphys.2013.07.052.
[85] S. Hertzman, R. Naraghi, S. Wessman, R. Pettersson, U. Borggren, J.Y. Jonsson, N. H. Pettersson, M.K. Karami, A. Kohan-Zade, Nitrogen solubility in alloy systems relevant to stainless steels, Metall. Mater. Trans. A 52 (9) (2021) 3811–3820, https://doi.org/10.1007/s11661-021-06343-0.
[86] S.P. Karunanithi, R.K. Arasappan, S.S. Nallathambi, An overview on additive manufacturing of duplex stainless steels: microstructure, mechanical properties, corrosion resistance, postheat treatment, and future perspectives, Steel Res. Int. 95 (12) (2024) 2400463, https://doi.org/10.1002/srin.202400463.